TRACING THE MASS-DEPENDENT STAR FORMATION HISTORY OF LATE-TYPE GALAXIES USING X-RAY EMISSION: RESULTS FROM THE CHANDRA DEEP FIELDS

B. D. LEHMER,[1,2] W. N. BRANDT,[1] D. M. ALEXANDER,[2] E. F. BELL,[3] A. E. HORNSCHEMEIER,[4] D. H. McINTOSH,[5] F. E. BAUER,[6] R. GILLI,[7] V. MAINIERI,[8,9] D. P. SCHNEIDER,[1] J. D. SILVERMAN,[9,10] A. T. STEFFEN,[1] P. TOZZI,[7] AND C. WOLF[11]

ABSTRACT

We report on the X-ray evolution over the last ≈ 9 Gyr of cosmic history (i.e., since $z = 1.4$) of late-type galaxy populations in the Chandra Deep Field–North and Extended Chandra Deep Field–South (CDF-N and E-CDF-S, respectively; jointly CDFs) survey fields. Our late-type galaxy sample consists of 2568 galaxies, which were identified using rest-frame optical colors and *HST* morphologies. We utilized X-ray stacking analyses to investigate the X-ray emission from these galaxies, emphasizing the contributions from normal galaxies that are not dominated by active galactic nuclei (AGNs). Over this redshift range, we find significant increases (factors of ≈ 5–10) in the X-ray–to–optical mean luminosity ratio (L_X/L_B) and the X-ray–to–stellar mass mean ratio ($L_X/M_\star$) for galaxy populations selected by L_B and $M_\star$, respectively. When analyzing galaxy samples selected via SFR, we find that the mean X-ray–to–SFR ratio (L_X/SFR) is consistent with being constant over the entire redshift range for galaxies with SFR = 1–100 $M_\odot$ yr^{-1}, thus demonstrating that X-ray emission can be used as a robust indicator of star formation activity out to $z \approx 1.4$. We find that the star formation activity (as traced by X-ray luminosity) per unit stellar mass in a given redshift bin increases with decreasing stellar mass over the redshift range $z = 0.2$–1, which is consistent with previous studies of how star formation activity depends on stellar mass. Finally, we extend our X-ray analyses to Lyman break galaxies at $z \sim 3$ and estimate that L_X/L_B at $z \sim 3$ is similar to its value at $z = 1.4$.

Subject headings: cosmology: observations — galaxies: active — galaxies: general — galaxies: spiral — stars: formation — surveys — X-rays: galaxies — X-rays: general

Online material: machine-readable tables

1. INTRODUCTION

Investigations focusing on global changes in star formation activity and stellar-mass build-up in field galaxies have provided significant insight into the physical evolution of galaxies and their constituent stellar populations. It has now been well established that the global star formation rate density has declined by roughly an order of magnitude since $z \approx 1$–1.5 (e.g., Lilly et al. 1996; Madau et al. 1996; Steidel et al. 1999; Hopkins 2004; Pérez-González et al. 2005; Schiminovich et al. 2005; Colbert et al. 2006). Recent investigations into the details of this evolution have shown that the star formation history of a given galaxy depends strongly on its stellar mass (e.g., Cowie et al. 1996; Juneau et al. 2005; Bundy et al. 2006; Noeske et al. 2007a, 2007b; Zheng

et al. 2007); the peak star formation epoch for the most massive galaxies occurred earlier in cosmic history than it did for galaxies with lower masses.

X-ray studies of normal late-type galaxies (i.e., those that are not dominated by luminous active galactic nuclei [AGNs]) have shown that X-ray emission provides a useful, relatively unobscured measure of star formation activity (e.g., Bauer et al. 2002a; Cohen 2003; Ranalli et al. 2003; Colbert et al. 2004; Grimm et al. 2003; Gilfanov et al. 2004a; Persic et al. 2004; Persic & Rephaeli 2007; however, see Barger et al. 2007). In normal galaxies, X-ray emission originates from X-ray binaries, supernovae, supernova remnants, hot (≈ 0.2–1 keV) interstellar gas, and O stars (see, e.g., Fabbiano 1989, 2006 for reviews). Sensitive *Chandra* and *XMM-Newton* studies of local late-type galaxies have shown that high-mass X-ray binaries (HMXBs) and low-mass X-ray binaries (LMXBs) typically dominate the total nonnuclear X-ray power output (e.g., Zezas et al. 2002; Bauer et al. 2003; Soria & Wu 2003; Swartz et al. 2003; Jenkins et al. 2005; Kilgard et al. 2005; however, see, e.g., Doane et al. 2004). Observations indicate that the integrated X-ray emission from HMXB and LMXB populations trace galaxy star formation rate (SFR) and stellar mass ($M_\star$), respectively. For example, using *Chandra* observations of 32 local galaxies, Colbert et al. (2004) found that the summed 0.3–8 keV nonnuclear point-source emission from a given galaxy (L_{XP}) can be approximated as $L_{XP} \approx \alpha\, M_\star + \beta\, \text{SFR}$, where α and β are constants. Therefore, galaxies having relatively high star formation rates per unit mass (specific star formation rates, SSFRs) generally have dominant X-ray point-source contributions from HMXBs (e.g., late-type star-forming galaxies), while those with relatively low SSFRs have point-source emission primarily from LMXBs (e.g., massive early-type galaxies).

If the X-ray binary populations are similarly dominating the normal-galaxy X-ray power output over a significant fraction of

[1] Department of Astronomy and Astrophysics, 525 Davey Lab, Pennsylvania State University, University Park, PA 16802.

[2] Department of Physics, University of Durham, South Road, Durham DH1 3LE, UK.

[3] Max-Planck-Institut für Astronomie, Königstuhl 17, D-69117 Heidelberg, Germany.

[4] Laboratory for X-Ray Astrophysics, NASA Goddard Space Flight Center, Code 662, Greenbelt, MD 20771.

[5] Astronomy Department, University of Massachusetts, 710 North Pleasant Street, Amherst, MA 01007.

[6] Columbia Astrophysics Laboratory, Columbia University, Pupin Laboratories, 550 West 120th Street, Room 1418, New York, NY 10027.

[7] Istituto Nazionale di Astrofisica (INAF)–Osservatorio Astrofisico di Arcetri, Largo E. Fermi 5, 50125 Firenze, Italy.

[8] European Southern Observatory, Karl-Schwarschild-Strasse 2, D-85748 Garching, Germany.

[9] Max-Planck-Institut für extraterrestrische Physik, Giessenbachstrasse, D-85748 Garching bei München, Germany.

[10] Institute of Astronomy, Department of Physics, Eidgenössische Technische-Hochschule, ETH Zurich, CH-8093, Switzerland.

[11] Department of Physics, University of Oxford, Keble Road, Oxford OX1 3RH, UK.

cosmic time, then there should be a rapid increase in the globally averaged X-ray luminosity of normal star-forming galaxies with cosmic look-back time in response to the increasing global star formation rate density (e.g., Ghosh & White 2001). In this scenario, HMXBs trace the immediate star formation rate of a galaxy and LMXBs trace its star formation history with a lag of a few Gyr. With the advent of deep *Chandra* and *XMM-Newton* surveys (see, e.g., Brandt & Hasinger 2005 for a review), it has become possible to study the X-ray properties of normal galaxies out to $z \gtrsim 1$ and $z \approx 0.3$, respectively (see, e.g., Hornschemeier et al. 2000, 2003; Alexander et al. 2002; Georgakakis et al. 2007; Georgantopoulos et al. 2005; Lehmer et al. 2006, 2007; Kim et al. 2006; Tzanavaris et al. 2006; Rosa-González et al. 2007). Evidence for a global increase in the X-ray activity with redshift for normal late-type galaxies has since been mounting. Studies of the X-ray luminosity functions of X-ray–detected normal galaxies have found that L_X^* evolves as $(1 + z)^{1.5–3}$ over the redshift range $z \approx 0$–1.4 (e.g., Norman et al. 2004; Ptak et al. 2007; Tzanavaris & Georgantopoulus 2008). In addition, X-ray stacking analyses have enabled investigations of more representative optically selected galaxy populations over the majority of cosmic history ($z \approx 0.1$–4; e.g., Brandt et al. 2001; Hornschemeier et al. 2002; Nandra et al. 2002; Georgakakis et al. 2003; Reddy & Steidel 2004; Laird et al. 2005, 2006; Lehmer et al. 2005a). These studies have found that the average X-ray luminosities of normal late-type galaxies increases with redshift out to $z \approx 1.4$–3. For example, using a ≈ 1 Ms exposure of a subregion within the Chandra Deep Field–North, Hornschemeier et al. (2002, hereafter H02) tentatively observed a factor of ≈ 2–3 increase in L_X/L_B from $z = 0$ to 1.4 for L_B^* galaxies. Despite these promising initial constraints, the details of the X-ray evolution of normal late-type galaxy populations, including dependences on the physical properties of galaxies (e.g., optical luminosity, stellar mass, environment, and star formation rate), have remained unexplored.

In this paper, we aim to improve significantly on constraints for the X-ray evolution of normal late-type galaxies (e.g., H02). We study for the first time how the X-ray properties of late-type field galaxies evolve as a function of optical luminosity, stellar mass, and star formation rate over the redshift range of $z = 0$–1.4. We construct late-type galaxy samples located in two of the most well-studied extragalactic X-ray survey fields, the ≈ 2 Ms Chandra Deep Field–North (CDF-N; Alexander et al. 2003) and the Extended Chandra Deep Field–South (E-CDF-S), which is composed of the central ≈ 1 Ms Chandra Deep Field–South (CDF-S; Giacconi et al. 2002) and four flanking ≈ 250 ks *Chandra* observations (Lehmer et al. 2005b). These Chandra Deep Fields (CDFs) reach 0.5–2 keV detection limits of $\approx 2.5 \times 10^{-17}$ ergs cm^{-2} s^{-1} in the most sensitive regions and $\lesssim 3 \times 10^{-16}$ ergs cm^{-2} s^{-1} over the majority of the CDFs; these levels are sufficient to detect moderately powerful X-ray sources ($L_{0.5–2 \text{ keV}} \gtrsim 10^{41.5}$ ergs s^{-1}) at $z = 1.4$ and $z = 0.6$, respectively. Therefore, the CDFs comprise an unprecedented data set for effectively studying the X-ray emission and evolution of cosmologically distant normal galaxies with minimal contamination from powerful AGNs.

The Galactic column densities are 1.3×10^{20} cm^{-2} for the CDF-N (Lockman 2004) and 8.8×10^{19} cm^{-2} for the E-CDF-S (Stark et al. 1992). All of the X-ray fluxes and luminosities quoted throughout this paper have been corrected for Galactic absorption. Unless stated otherwise, we quote optical magnitudes based on the AB magnitude system for *HST* photometry and the Vega magnitude system everywhere else. In the X-ray band, we make use of three standard bandpasses: 0.5–2 keV (soft band [SB]), 2–8 keV (hard band [HB]), and 0.5–8 keV (full band [FB]). Throughout this paper, we make estimates of stellar mass and

star formation rates using a Kroupa (2001) initial mass function (IMF); when making comparisons between these estimates and those quoted in other studies, we have adjusted all values to correspond to our adopted IMF. $H_0 = 70$ km s^{-1} Mpc^{-1}, $\Omega_M = 0.3$, and $\Omega_\Lambda = 0.7$ are adopted throughout this paper (e.g., Spergel et al. 2003), which imply a look-back time of 7.7 Gyr at $z = 1$.

2. LATE-TYPE GALAXY SAMPLE SELECTION

We constructed an optically selected sample of late-type galaxies within the CDFs to use for our subsequent analyses. We restricted our galaxy selection to regions of the CDFs where *Hubble Space Telescope* (*HST*) observations were available to allow the best possible morphological classifications. The *HST* observations in the CDFs have been carried out via the Great Observatories Origins Deep Survey (GOODS; Giavalisco et al. 2004a) and Galaxy Evolution from Morphology and SEDs (GEMS; Rix et al. 2004; Caldwell et al. 2005) programs; these surveys cover $\approx 90\%$ of the *Chandra*-observed regions of the CDFs with the Advanced Camera for Surveys (ACS). In the GOODS and GEMS regions, photometry was available for four (B_{435}, V_{606}, i_{775}, and z_{850}) and two (V_{606} and z_{850}) ACS passbands, respectively.

2.1. *Galaxy Selection Footprint*

We began building our sample by selecting all galaxies having $z_{850} < 23$. This initial selection criterion was motivated by (1) the availability of deep z_{850}-band imaging over all of the CDFs, (2) the fact that the z_{850} emission probes mass-tracing rest-frame optical light redward of the 4000 Å break for galaxies at $z \lesssim 1$, which constitutes the large majority of our sample, (3) the availability of reliable spectroscopic and photometric redshifts (see details below), and (4) the high multiwavelength detection fractions for these sources, which allow us to determine informative rest-frame spectral energy distributions (SEDs). In order to isolate most effectively distant X-ray–detected AGNs, we further restricted our sample to include only galaxies that were located in the most sensitive areas of the CDFs where the *Chandra* point-spread function (PSF) was small. We therefore chose to include sources having optical positions that were within 6.0′ of at least one of the six *Chandra* aim points in the CDFs;[12] the corresponding total areal footprint is ≈ 0.18 deg^2. Futhermore, we removed obvious Galactic stars that were identified via optical spectral properties or the presence of obvious diffraction spikes in the z_{850}-band images. Under these restrictions, we found 6905 galaxies.

2.2. *Redshifts*

We cross-correlated our initial sample of 6905 galaxies with available spectroscopic and photometric redshift catalogs (e.g., Barger et al. 2003; Le Fèvre et al. 2004; Szokoly et al. 2004; Wirth et al. 2004; Wolf et al. 2004; Mobasher et al. 2004; Mignoli et al. 2005; Vanzella et al. 2005, 2006; Grazian et al. 2006; Ravikumar et al. 2007; J. D. Silverman et al. 2008, in preparation). All galaxies that did not have spectroscopic redshifts were located in the E-CDF-S where highly accurate (median $\delta z/1 + z \approx 0.02$ for galaxies with $z_{850} < 23$) photometric redshifts were available via COMBO-17 (Classifying Objects by Medium-Band Observations in 17 Filters; Wolf et al. 2004). In total, 6683 ($\approx 97\%$) of our sources had either spectroscopic or photometric redshifts. Visual inspection of the 222 galaxies in the E-CDF-S without

---

[12] For the CDF aim points, see Tables 1 and A1 of Alexander et al. (2003) for the ≈ 2 Ms CDF-N and ≈ 1 Ms CDF-S, respectively, as well as Table 1 of Lehmer et al. (2005b) for the ≈ 250 ks E-CDF-S.

redshifts indicated that these sources were mainly faint galaxies near bright stars, as well as a handful of sources that were subgalactic features within relatively nearby galaxies.

Whenever possible, we adopted spectroscopic redshifts as the most accurate redshifts for our galaxies. Using the redshift information, we filtered our sample to include only sources with $z < 1.4$ in the ≈ 2 Ms CDF-N, $z < 1$ in the ≈ 1 Ms CDF-S, and $z < 0.6$ in the ≈ 250 ks regions of the E-CDF-S; these redshift limits represent the largest distances at which we would expect to identify moderately luminous ($L_{0.5-2\,keV} \gtrsim 10^{41.5}$ ergs s^{-1}) AGNs effectively in each respective field. In total, 3259 galaxies remained after filtering our sample based on redshift properties. We used spectroscopic redshifts for 1351 ($\approx 41\%$) galaxies and photometric redshifts for the remaining 1908 ($\approx 59\%$) galaxies.

2.3. Rest-Frame Color and Morphological Selection

The optical-color distribution for field galaxies has been shown to be bimodal, separating "red" and "blue" galaxy populations (e.g., Strateva et al. 2001; Hogg et al. 2002b; Blanton et al. 2003; Baldry et al. 2004). Studies of the color-magnitude relation for distant galaxy populations have shown that this color bimodality is observed to persist out to at least $z \approx 1-1.5$ (see, e.g., Bell et al. 2004a; Faber et al. 2007; Labbé et al. 2007), thus providing an excellent quantifiable means for separating late-type and early-type galaxy populations. We therefore filtered our galaxy sample to include only sources that had blue rest-frame optical colors, as expected for late-type galaxies that contain young stellar populations. To estimate rest-frame $U - V$ colors and absolute U-, B-, and V-band magnitudes (M_U, M_B, and M_V, respectively) for each of the 3259 galaxies in our sample, we utilized the available optical/near-IR data.

For the CDF-N, we used the U, B, V, R, I, z', and HK' photometric catalogs from Capak et al. (2004), as well as *Spitzer* IRAC imaging (3.6, 4.5, 5.8, and 8.0 μm; Fazio et al. 2004) from the GOODS (M. Dickinson et al., in preparation). For the E-CDF-S, we used (1) the 17-bandpass photometry available through COMBO-17, (2) J and K_s imaging from the ESO Imaging Survey (Olsen et al. 2006), (3) J, H, and K from the MUSYC collaboration (E. N. Taylor et al., in preparation; see also Moy et al. 2003; Gawiser et al. 2006), and (4) *Spitzer* IRAC data from the GOODS and SIMPLE teams (M. Dickinson et al., in preparation; P. G. van Dokkum et al., in preparation). Using these data, we constructed a rest-frame near-UV–to–near-IR SED for each galaxy. For these SEDs, the rest-frame U, B, and V filters are well sampled at all relevant redshifts, with the exception of sources at $z \gtrsim 0.7$, where the wavelength range of the available data is sparse at rest-frame V band. For sources at $z \gtrsim 0.7$, we linearly interpolated our SED to cover the V filter. We convolved these SEDs with Johnson U-, B-, and V-filter curves and computed rest-frame absolute magnitudes for each respective filter following equation (5) of Hogg et al. (2002a). For sources in the E-CDF-S, these computed absolute magnitudes are consistent with those presented by Wolf et al. (2004).

In Figure 1 (*small filled circles*), we present rest-frame $U - V$ colors versus M_V for our galaxies in six redshift ranges. For clarity, we also show inset histograms giving the distribution of rest-frame $U - V$ colors for each redshift interval. We utilized the rest-frame $U - V$ color to divide roughly populations of red and blue galaxies. Use of the rest-frame $U - V$ color was motivated by Bell et al. (2004a), who note that the U and V bandpass pair straddle the 4000 Å break, which is particularly sensitive to age and metallicity variations of galactic stellar populations. The dashed lines in Figure 1 show the empirically determined redshift-dependent color divisions that separate blue and red galaxy

populations; we calculated these divisions following § 5 of Bell et al. (2004a):

$$(U - V)_{rest} = 1.15 - 0.31z - 0.08(M_V + 20.7). \qquad (1)$$

Galaxies having rest-frame $U - V$ less than the values provided by equation (1) are often referred to as "blue cloud" galaxies, while those with rest-frame $U - V$ greater than the division are called "red sequence" galaxies. The redshift dependence of the blue-cloud/red-sequence galaxy division is thought to be largely due to the evolution of the mean age and dust content of the blue-cloud population, with a smaller contribution from changes in metallicity. In total, we found 2502 blue-cloud galaxies and 757 red-sequence galaxies.

Generally, the blue-cloud and red-sequence populations are composed of late-type and early-type galaxies, respectively (see, e.g., Bell et al. 2004b, 2005; McIntosh et al. 2005). In support of this point, we have created Figure 2, which shows the fraction of E-CDF-S galaxies in our sample having blue-cloud (*dashed histogram*) and red-sequence (*dotted histogram*) colors as a function of galaxy Sérsic index n. We utilized the Häußssler et al. (2007) Sérsic indices, which were computed using the GEMS z_{850} images and the GALFIT (Peng et al. 2002) two-dimensional light-profile fitting program. Light-profile studies of large galaxy samples have found empirically that a Sérsic cutoff of $n = 2.5$ can roughly discriminate between late-type and early-type galaxies (e.g., Blanton et al. 2003; Shen et al. 2003; Hogg et al. 2004). Galaxies with $n \lesssim 2.5$ are generally late-type galaxies, while the majority of galaxies with $n \gtrsim 2.5$ are early-types (vertical line in Fig. 2). Figure 2 shows that there is reasonable agreement between late-type and early-type galaxy populations selected using rest-frame optical colors and Sérsic indices.

We refined further our division between late-type and early-type morphologies by visually inspecting the z_{850}-band images of our entire sample of 3259 galaxies to see if there were obvious cases where the rest-frame optical colors provided an inaccurate morphological classification. For example, late-type galaxies that are highly inclined to our line of sight may experience significant reddening of the young (and blue) disk population and will have red-sequence colors. Also, due to variations of the stellar populations in galaxies of a given morphological class, there will be some scatter in rest-frame $U - V$ color near the division of the red-sequence and blue-cloud regimes. This will lead to a number of "green" galaxies that are misclassified morphologically when the classification is based solely on rest-frame color. We stress that such a visual inspection is only to correct source classifications that were *obviously misclassified* by simply using color-magnitude diagrams, and our resulting sample should not be considered a morphologically selected sample.

Based on our visual inspection, we found 76 obvious early-type galaxies with blue-cloud colors, and 142 obvious late-type galaxies with red-sequence colors; we reclassified these sources as late-type and early-type galaxies, respectively. We inspected histograms of the fraction of blue-cloud and red-sequence galaxies that were reclassified as a function of redshift and find no obvious redshift-related trend. In Figure 3, we show z_{850}-band postage-stamp images of 10 obvious early-type galaxies with blue-cloud colors (*top panels*), as well as 10 obvious late-type galaxies with red-sequence colors (*bottom panels*). After reclassifying these objects, we were left with 2568 late-type galaxies and 691 early-type galaxies with $z = 0-1.4$. Since we were interested in studying the properties of the late-type galaxy populations, we hereafter refer to our sample of 2568 late-type galaxies as our *main sample*, which we use in subsequent analyses.
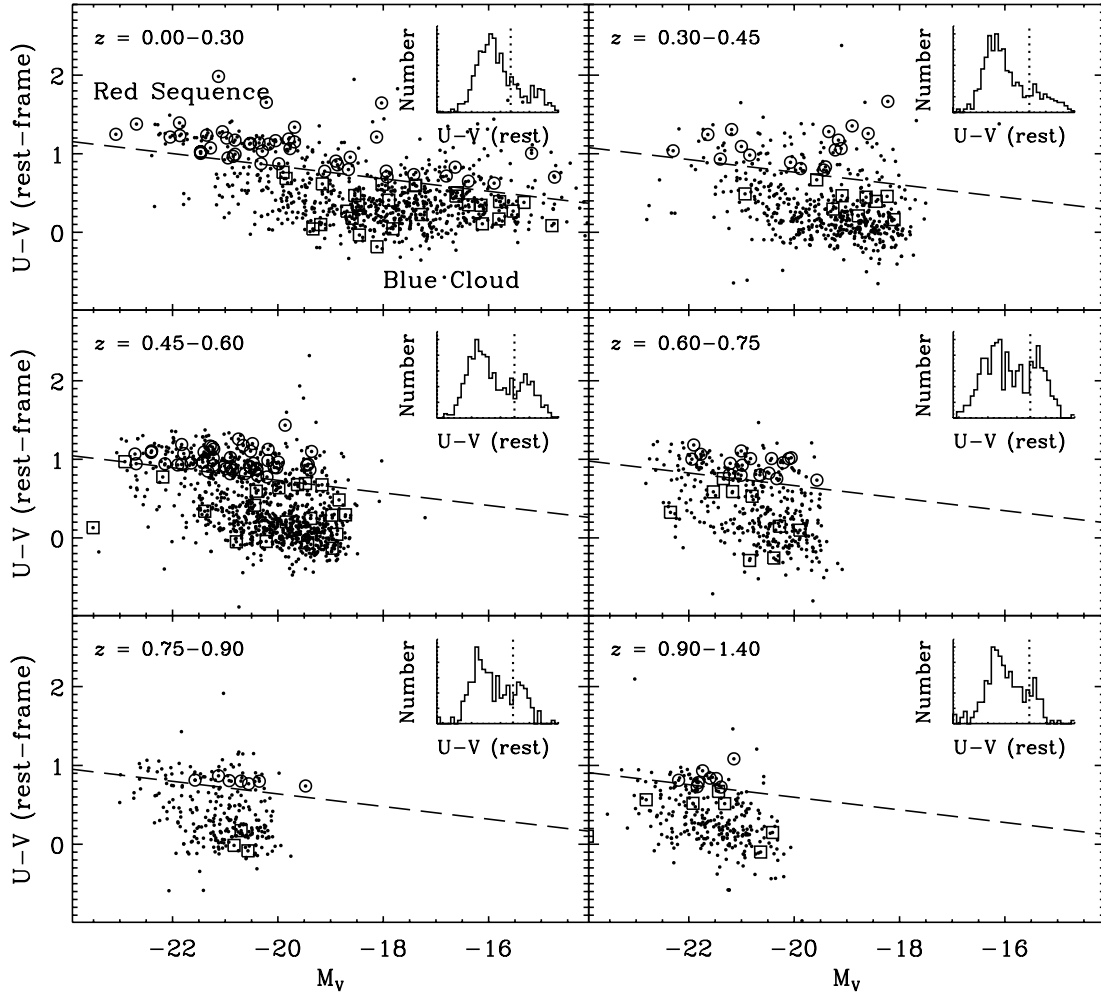
Fig. 1.—Rest-frame $U - V$ color vs. absolute V-band magnitude M_V (color-magnitude diagrams) for the 3259 $z \approx 0$–1.4 galaxies with $z_{850} < 23$ that were within 6.0′ of at least one CDF aim point. Each panel shows the color-magnitude relation for a given redshift bin (annotated in the upper left-hand corners). The dashed line in each panel represents the estimated division between red (large $U - V$ values) and blue (small $U - V$ values) galaxy populations, which was estimated using eq. (1) and the median redshift of the galaxies in each bin. Open symbols highlight red-sequence and blue-cloud galaxies that were visually reclassified as late-type (*open circles*) and early-type (*open squares*) galaxies, respectively. The inset histogram in each panel shows the distribution of rest-frame $U - V$. The vertical dotted line in each inset plot indicates the estimated division between red and blue galaxy populations, which was calculated using eq. (1) and the median redshift and M_V for galaxies in each redshift bin (see § 2.3).
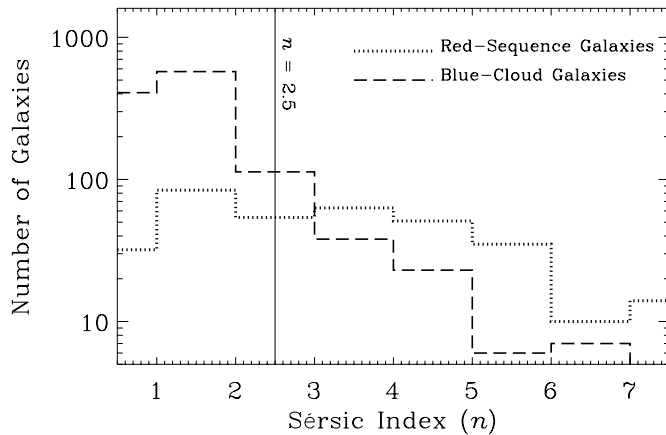

Fig. 2.—Distribution of Sérsic indices (n) for our initial sample of $z = 0$–1 galaxies in the E-CDF-S having blue-cloud (*dashed histogram*) and red-sequence (*dotted histogram*) colors. The solid vertical line indicates $n = 2.5$, the empirical cutoff between late-type ($n \lesssim 2.5$) and early-type galaxies ($n \gtrsim 2.5$).

3. PHYSICAL PROPERTIES AND REDSHIFT EVOLUTION OF LATE-TYPE GALAXIES

The primary goal of this study is to investigate the X-ray evolution of normal (i.e., non-AGN) late-type galaxies and to determine how this evolution depends on three intrinsic physical properties: optical luminosity, stellar mass, and star formation rate. Below, we describe how we estimated each of these physical properties for the galaxies in our main sample. We note that the populations of late-type galaxies that we are investigating here have been selected via their intrinsic physical properties, which may have changed significantly from the observed epoch to the present day. For example, it is expected that a significant fraction of the late-type galaxies in our main sample will evolve into early-type galaxies via mergers or passive stellar evolution (e.g., Bell et al. 2007). Ideally, we would like to study the evolution of the X-ray properties of late-type galaxies while controlling for such changes in the physical nature of each galaxy. However, since the details of this evolution are highly complex and not well understood for a given galaxy, such a task is beyond the scope of this paper. We therefore investigate the X-ray evolution of normal
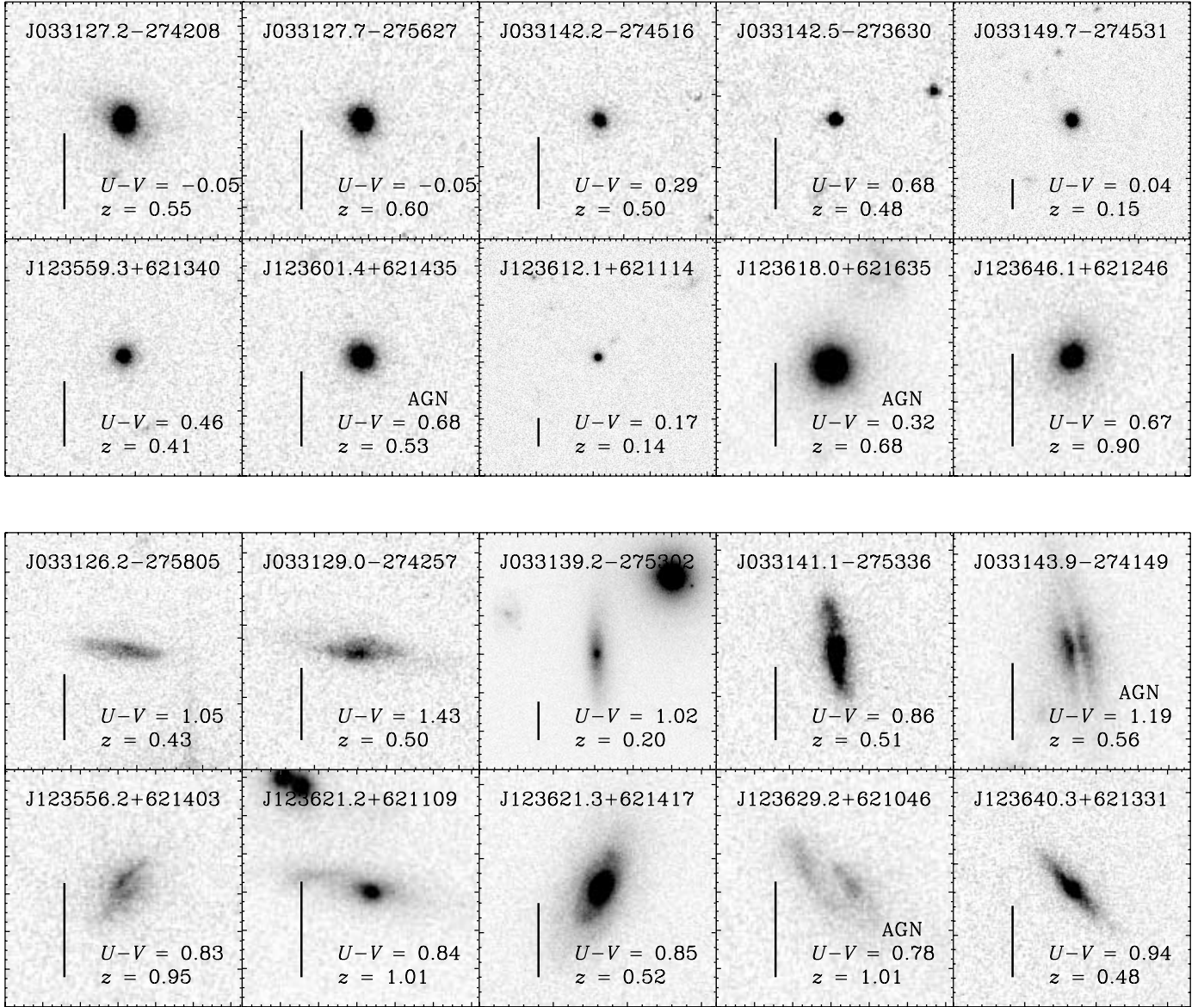
FIG. 3.—*HST* Advanced Camera for Surveys (ACS) z_{850} example images of 10 blue-cloud galaxies that have obvious early-type morphologies (*top panel*) and 10 red-sequence galaxies that have obvious late-type morphologies (*bottom panel*); these images demonstrate the aid of the *HST* coverage. Each postage-stamp image has a physical size of 30 kpc × 30 kpc, and in each image we indicate the source name (*top*), the rest-frame $U - V$ color and redshift of the source (*lower right*), and a vertical bar of length 1.5″ for scaling reference (*lower left*); sources harboring an X-ray–detected AGN (see § 4.1) have been annotated with the label "AGN" in the lower right.

late-type galaxy populations in relation to their observed intrinsic physical properties.

3.1. *Optical Luminosity*

In order to study late-type galaxy samples selected using an observable quantity, we made use of the B-band luminosity (L_B). In § 2.3, we computed absolute B-band magnitudes M_B for galaxies in our main sample using photometrically derived SEDs. The B-band emission from a given late-type galaxy will be significantly influenced by large populations of old ($\gtrsim 100$ Myr) stars (measured by the stellar mass) as well as the younger and less-numerous massive stars that reside in low-obscuration star-forming regions (measured by the star formation rate). In Figure 4a, we show L_B (expressed in solar units; where $L_{B,\odot} = 5.2 \times 10^{32}$ ergs s^{-1}) versus redshift for galaxies in our main sample. The redshift-dependent selection limit of L_B for our sample is set by our $z_{850} < 23$ criterion, and at $z = 0.5$ ($z = 1.4$) this limit corresponds to roughly $L_B \approx 3 \times 10^9$ $L_{B,\odot}$ ($L_B \approx 4 \times 10^{10}$ $L_{B,\odot}$).

For comparison, in Figure 4a we have plotted the values of L_B for the Milky Way (MW) and local galaxies M101, M82, and NGC 3256. For the MW, we adopted $L_B = 1.9 \times 10^{10}$ $L_{B,\odot}$ as the approximate total disk-plus-bulge B-band luminosity (see Table 15.2 of Gilmore et al. 1990). For the local galaxies, we utilized optical photometry from the Third Reference Catalog of Bright Galaxies (RC3; de Vaucouleurs et al. 1991) and adopted distances from the *IRAS* Revised Galaxy Sample (Sanders et al. 2003), which gives distances of 6.7, 3.6, and 35.4 Mpc and implies corresponding B-band luminosities of 3.3×10^{10}, 3.8×10^9, and 4.8×10^{10} $L_{B,\odot}$ for M101, M82, and NGC 3256, respectively.

3.2. *Stellar Mass*

As discussed in § 1, the X-ray emission from LMXB populations scales with galaxy stellar mass. It is therefore useful to select late-type galaxies via their stellar masses as a means for estimating the LMXB contribution to their X-ray emission. To estimate the stellar mass ($M_\star$) of each of our galaxies, we exploited
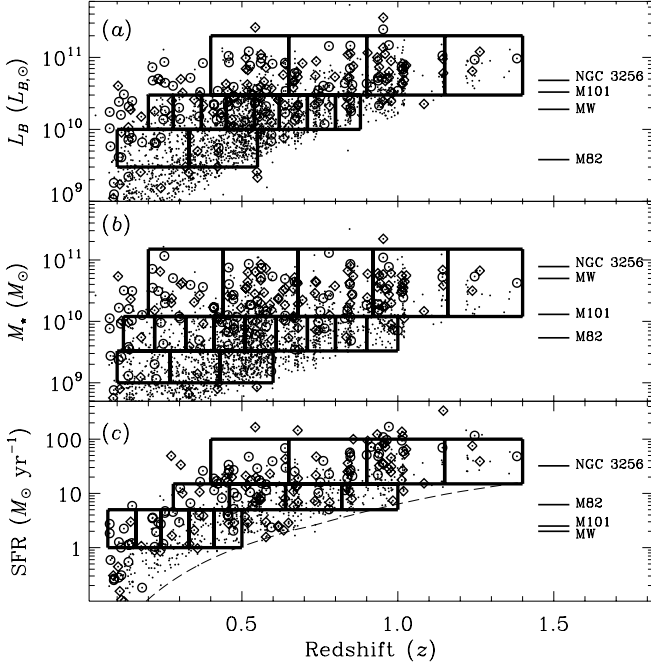
FIG. 4.—(a) Rest-frame B-band luminosity L_B, (b) stellar mass $M_\star$, and (c) star formation rate SFR vs. redshift for sources in our main sample. For comparison, in each panel we have indicated the properties of the MW and local galaxies M101, M82, and NGC 3256. In (c), we have included only SFRs for the 888 late-type galaxies in our main sample that have 24 μm counterparts (see § 3.3 for details); the dashed curve indicates roughly the SFR detection limit for sources without 24 μm counterparts. X-ray–detected normal galaxies and AGNs have been indicated with open circles and diamonds, respectively. The thick gray rectangles indicate regions where galaxy populations were selected for X-ray stacking (see §§ 4.2 and 5.1). For each galaxy, $M_\star$ and SFR were computed following eqs. (2) and (3), respectively.

the tight correlation between rest-frame optical color and stellar mass-to-light ratio (e.g., Bell & de Jong 2001; Bell et al. 2003; Kauffmann et al. 2003a; see also Borch et al. 2006). For this calculation, we used a combination of rest-frame $B - V$ colors and rest-frame K-band luminosities. K-band luminosities were computed by fitting all available optical/near-IR photometric data to a grid of 276 synthetic spectra generated by the PÉGASE stellar population synthesis code (Fioc & Rocca-Volmerange 1997). These templates assume a single formation epoch with an exponentially decaying star formation history (time constants $\tau = 1, 2, 4,$ and 7 Gyr) and a Kroupa et al. (1993) IMF; the template grid spans ages of 0–15 Gyr. For each galaxy in our main sample, we convolved the best-fit template spectrum with the K-band filter function to approximate the rest-frame K-band luminosity, L_K. This method allowed us to account for significant curvature in the rest-frame near-IR SEDs of our sources where photometric data points did not always overlap with the rest-frame K band. We note that 2546 ($\approx$99.1%) of our late-type galaxies have at least one photometric data point lying at rest-frame wavelengths between 1 and 6 μm, which significantly constrains the SED in the rest-frame K band. We adopted the prescription outlined in Appendix 2 of Bell et al. (2003) to estimate $M_\star$ using rest-frame $B - V$ color and K-band luminosity:

$$\log M_\star/M_\odot = \log L_K/L_{K,\odot} + 0.135(B - V) - 0.306. \quad (2)$$

The numerical constants in equation (2) were supplied by Table 7 of Bell et al. (2003) and are appropriate for our choice of $B - V$ color and L_K; the normalization has been adjusted by -0.1 dex to account for our adopted Kroupa (2001) IMF (see § 1). We com-

pared our stellar-mass estimates with those computed by Borch et al. (2006) for 1758 ($\approx$68% of our main sample) galaxies in the COMBO-17 survey and find excellent agreement between methods, with an overall scatter of $\approx$0.2 dex.

In Figure 4b, we show $M_\star$ versus redshift for our sample of late-type galaxies. We note that our stellar-mass estimates are broadly limited by the $z_{850} < 23$ criterion used in our sample selection. At $z = 0.5$ ($z = 1.4$) our samples are representative for late-type galaxies with $M_\star \gtrsim 10^9 M_\odot$ ($M_\star \gtrsim 10^{10} M_\odot$). For comparison, in Figure 4b we have plotted stellar masses for the MW and local galaxies M101, M82, and NGC 3256. We adopted a stellar mass of $5 \times 10^{10} M_\odot$ for the MW (e.g., Hammer et al. 2007). For the local galaxies, we estimated $M_\star$ using a similar relation to equation (2), except using $B - V$ color and B-band luminosity (see Appendix 2 of Bell et al. 2003 for details); for this computation, we utilized $B - V$ colors from RC3 and values of L_B determined in § 3.1. This computation gives stellar masses of 1.3×10^{10}, 5.4×10^9, and $7.8 \times 10^{10} M_\odot$ for M101, M82, and NGC 3256, respectively.

3.3. Star Formation Rates

Since the X-ray emission from normal late-type galaxies is known to be strongly correlated with SFR, it is of particular interest to understand how changes in SFR have contributed to the X-ray evolution of the normal late-type galaxy population. To calculate SFRs for the galaxies in our main sample, we utilized estimates of both the dust-uncorrected ultraviolet luminosities (L_{UV}) originating from young stars and the infrared luminosities (8–1000 μm; L_{IR}) from the dust that obscures UV light in star-forming regions (see, e.g., Kennicutt 1998 for a review). The former quantity was computed following $L_{UV} = 3.3\nu l_\nu(2800 \text{ Å})$, where $l_\nu(2800 \text{ Å})$ is the rest-frame 2800 Å monochromatic luminosity (see § 3.2 of Bell et al. 2005); $l_\nu(2800 \text{ Å})$ was approximated using the template SEDs that were constructed in § 3.2. The latter quantity (L_{IR}) was computed using observed-frame 24 μm flux densities (i.e., rest-frame 24 μm/1 + z) from observations with the MIPS (Rieke et al. 2004) camera on board *Spitzer*. We note that generally the dust-obscured star formation activity, probed here using L_{IR}, can be measured using either the UV spectral slope or optical nebular recombination lines (e.g., Balmer emission lines and O II); however, the data available for our $z \approx 0$–1.4 late-type galaxies lack the rest-frame UV and spectroscopic coverage needed to provide such useful measurements.

Over the CDFs, deep 24 μm observations were available for the GOODS fields ($f_{24\mu m,\text{lim}} \approx 30 \mu$Jy, 6 σ).[13] For the remaining area (covering the outer regions of the E-CDF-S), shallower 24 μm observations ($f_{24\mu m,\text{lim}} \approx 120 \mu$Jy) were available through SWIRE (Lonsdale et al. 2003). We matched the positions of the 2568 late-type galaxies in our main sample with those from the available 24 μm source catalogs, requiring that the *HST* and *Spitzer* centroids be offset by no more than 1.5″. We found successful matches for 888 ($\approx$35%) of our late-type galaxies. For these sources, we converted 24 μm flux densities to L_{IR} following the methods outlined in Papovich & Bell (2002). Briefly, we utilized the entire grid of 64 infrared SEDs provided by Dale et al. (2001) to estimate the mean conversion factor $\eta(z)$, which transforms observed-frame 24 μm luminosity $\nu l_\nu(24 \mu$m/1 + z) to L_{IR} as a function of redshift [i.e., $L_{IR} = \eta(z)\nu l_\nu(24\mu$m/1 + z)]. The mean conversion factor spans the tight range of $\eta = 7.2$–12.2 over the entire redshift range $z = 0$–1.4. We note that different choices of infrared SEDs yield similar results at $z \lesssim 1$, but become significantly discrepant at $z \gtrsim 1$ (see, e.g., Fig. 2 of Papovich & Bell 2002).

---

[13] Available at http://ssc.spitzer.caltech.edu/legacy/goodshistory.html.

Using our estimates of L_{UV} and L_{IR}, we calculated star formation rates for galaxies in our sample using the following equation:

$$\mathrm{SFR}(M_\odot \ \mathrm{yr}^{-1}) = 9.8 \times 10^{-11}(L_{IR} + L_{UV}), \qquad (3)$$

where L_{IR} and L_{UV} are expressed in units of the solar bolometric luminosity ($L_\odot = 3.9 \times 10^{33}$ ergs s^{-1}). Equation (3) was adopted from § 3.2 of Bell et al. (2005) and was derived using PÉGASE stellar-population models, which assumed a 100 Myr old population with constant SFR and a Kroupa (2001) IMF (see Bell 2003 for further details). We note that for the majority of our galaxies $L_{IR} > L_{UV}$, and for sources with $z \leq 0.5$ and $z > 0.5$, the median IR-to-UV ratio $L_{IR}/L_{UV} = 2.8$ and 7.1, respectively. Our $z \leq 0.5$ galaxies have median $L_{IR} = 1.1 \times 10^{10} \ L_\odot$, which is characteristic of objects that are found in the nearby $D < 10$ Mpc universe. By contrast, our $z > 0.5$ galaxies have median $L_{IR} = 9.3 \times 10^{10} \ L_\odot$, similar to the local LIRG population found at $D > 10$ Mpc. In Figure 4c, we show the distribution of SFRs for the 888 galaxies in our main sample that had 24 μm counterparts. We note that for sources in our main sample that were within the GOODS regions, where the 24 μm observations are most sensitive, the infrared detection fraction drops from $\approx$100% for galaxies with $z_{850} = 20 \pm 0.2$ to $\approx$20% for galaxies with $z_{850} = 22.8 \pm 0.2$. This demonstrates that our SFR completeness is limited primarily by the 24 μm sensitivity limit and that our sample of $z_{850} < 23$ late-type galaxies is highly representative of galaxy populations above the apparent redshift-dependent SFR limit shown in Figure 4c (dashed curve). At $z = 0.5$ ($z = 1.4$), this limit corresponds to SFR $\approx 1 \ M_\odot \ \mathrm{yr}^{-1}$(SFR $\approx 15 \ M_\odot \ \mathrm{yr}^{-1}$). For comparison, in Figure 4c we have plotted the SFRs for the MW and local galaxies M101, M82, and NGC 3256. The SFR of the MW was taken to be $\approx 2 \ M_\odot \ \mathrm{yr}^{-1}$ (McKee & Williams 1997), and the SFRs of the local galaxies were computed using equation (3). Values of $l_\nu(2800$ Å$)$ were approximated from SEDs available through the NASA/IPAC Extragalactic Database (NED)[14] and L_{IR} was taken from the *IRAS* Revised Bright Galaxy Sample (Sanders et al. 2003). We find SFR = 2.5, 6.2, and 32.2 $M_\odot \ \mathrm{yr}^{-1}$ for M101, M82, and NGC 3256, respectively.

As a consistency check on our UV-plus-infrared SFR estimates SFR(UV+IR), we calculated radio-derived SFRs using 1.4 GHz observations, SFR(1.4 GHz), following equation (7) of Schmitt et al. (2006), which we adjusted to be consistent with our adopted Kroupa (2001) IMF. We matched sources in our main sample to 1.4 GHz catalogs, which were derived from observations using the VLA in the CDF-N ($\approx$30 μJy; Richards et al. 1998) and the ATCA in the E-CDF-S ($\approx$60 μJy; Afonso et al. 2006; Rovilos et al. 2007). Using a matching radius of 1.5$''$, we found a total of 54 radio sources coincident with our late-type galaxies. We found that 48 ($\approx$89%) of the radio-detected sources had 24 μm counterparts, allowing for reasonable comparison between derived SFRs. For these sources we found reasonable agreement between SFRs derived from UV-plus-infrared and radio measurements, with a mean ratio of SFR(1.4 GHz)/SFR(UV+IR) = 1.5 $\pm$ 1.0. A large number of late-type galaxies (840 sources) in our main sample were detected in the 24 μm observations that were not detected at 1.4 GHz. All but three of these sources had SFR(1.4 GHz) upper limits that were consistent with that expected from estimates of SFR(UV+IR) (see § 4.1 for further details).

4. ANALYSIS

4.1. *X-Ray−Detected Late-Type Galaxies and AGN Identification*

We utilized the multiwavelength observations in the CDFs to obtain a census of the active galaxies in our main sample. We

began by matching the optical positions of our galaxies to the X-ray positions of point sources in the CDF catalogs of Alexander et al. (2003)[15] for the $\approx$2 Ms CDF-N and $\approx$1 Ms CDF-S and Lehmer et al. (2005b)[16] for the $\approx$250 ks E-CDF-S. For a successful match, we required that the optical and X-ray centroids be displaced by no more than 1.5 times the radius of the *Chandra* positional error circles (80%−90% confidence), which are provided in each respective catalog. We note that for a small number of the galaxies in our sample at $z \lesssim 0.3$, moderately luminous off-nuclear X-ray sources (e.g., ultraluminous X-ray sources [ULXs]) that are intrinsically related to the galaxies may lie outside of our adopted matching radius; we utilized the off-nuclear X-ray source catalog of Lehmer et al. (2006) to identify such galaxies and assign X-ray properties (see details below).

The *Chandra* source catalogs were generated using `wavdetect` (Freeman et al. 2002) with false-positive probability thresholds of 1×10^{-7} and 1×10^{-6} for the Alexander et al. (2003) and Lehmer et al. (2005b) point-source catalogs, respectively. However, as demonstrated in § 3.4.2 of Alexander et al. (2003) and § 3.3.2 of Lehmer et al. (2005b), legitimate lower significance X-ray sources, detected by running `wavdetect` at a false-positive probability threshold of 1×10^{-5}, can be isolated by matching with relatively bright optical sources; therefore, when matching our late-type galaxies to X-ray−detected sources, we utilized this technique. The sky surface density for late-type galaxies in our main sample ranges from $\approx$23,000 deg^{-2} in the CDF-N to $\approx$8800 deg^{-2} in the $\approx$250 ks E-CDF-S. The large difference between these source densities is primarily due to differences in applied redshift cuts (see § 2.2). Given the fact that the positional uncertainties are generally small ($\lesssim$1.5$''$) for sources within 6.0$'$ of the *Chandra* aim points, as is the case for sources in our main sample, the corresponding estimated number of spurious matches is small. We estimate that when using `wavdetect` with a false-positive probability threshold of 1×10^{-5} to search for sources in three *Chandra* bandpasses (0.5–2 keV, 2–8 keV, and 0.5–8 keV), we expect $\approx$1.8 spurious matches. When including the off-nuclear sources from Lehmer et al. (2006), we expect an additional $\approx$0.5 false sources; this brings our total spurious matching estimate to $\approx$2.3 sources for our main sample.

Using the matching criteria above, we find that 225 late-type galaxies are detected in at least one of the 0.5–2 keV, 2–8 keV, or 0.5–8 keV bandpasses. Out of these 225 galaxies, 12 are known off-nuclear X-ray sources from Lehmer et al. (2006). Since only one off-nuclear source is detected for each host galaxy, we assume that the off-nuclear point-source dominates the total X-ray emission from each host galaxy. We therefore adopted the X-ray properties presented in Table 1 of Lehmer et al. (2006) for each off-nuclear host galaxy.

The unprecedented depths of the CDFs allow for the individual X-ray detection of luminous normal galaxies over the entire redshift range of our main sample ($z = 0$–1.4); however, the majority of the X-ray−detected sources in even the most sensitive regions of the CDFs will be distant ($z \gtrsim 0.5$) AGNs (e.g., Bauer et al. 2004), which we want to separate from our normal late-type galaxy sample. We identified AGN candidates using four primary criteria, which utilize (1) X-ray hardness to identify luminous obscured sources, (2) X-ray−to−optical flux ratios to identify additional relatively unobscured AGNs, (3) the X-ray−SFR correlation to identify additional lower luminosity AGNs that are significantly

---

[14] Available at http://nedwww.ipac.caltech.edu/.

[15] See http://www.astro.psu.edu/users/niel/hdf/hdf-chandra.html for the relevant source catalogs and data products for the $\approx$2 Ms CDF-N and $\approx$1 Ms CDF-S.

[16] See http://www.astro.psu.edu/users/niel/ecdfs/ecdfs-chandra.html for the relevant source catalogs and data products for the $\approx$250 ks E-CDF-S.
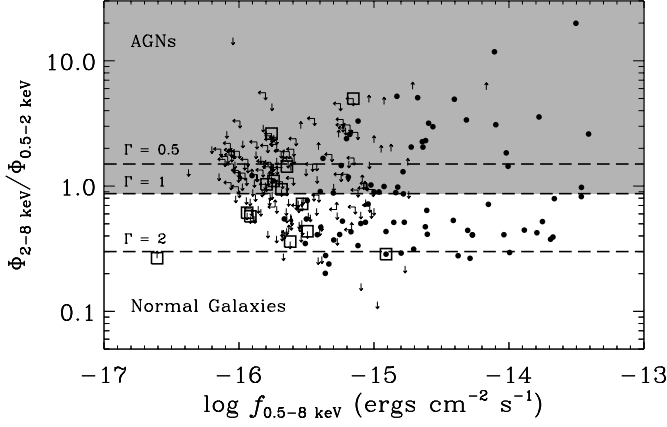
Fig. 5.—Count-rate ratio in the 2–8 keV to 0.5–2 keV bandpasses ($\Phi_{2-8\,keV}/\Phi_{0.5-2\,keV}$) vs. the logarithm of the 0.5–8 keV flux ($\log f_{0.5-8\,keV}$) for X-ray–detected sources in our main sample. Off-nuclear X-ray sources cataloged by Lehmer et al. (2006) have been highlighted with open squares. The shaded region represents sources with effective photon indices $\Gamma_{eff} \lesssim 1$; we classified these sources as AGN candidates (see § 4, criterion 1). For reference, we have plotted lines corresponding to $\Gamma_{eff} = 0.5$, 1, and 2 (dashed lines).

Fig. 6.—R-band magnitude vs. $\log f_{0.5-8\,keV}$ for X-ray–detected sources in our main sample. Open circles represent sources that were classified as AGN candidates by criterion 1 (see § 4.1 and Fig. 5), and filled circles represent all other sources; open squares have the same meaning as in Fig. 5. The shaded area represents the region where $\log(f_{0.5-8\,keV}/f_R) > -1$; we classified sources in this region as AGN candidates (see § 4.1, criterion 2). For reference, the dashed lines represent $\log(f_{0.5-8\,keV}/f_R) = -2$, -1, and 1.

influencing the total X-ray emission, and (4) the combination of radio and infrared properties to identify additional Compton-thick AGNs and radio-loud AGNs. As a final check on our AGN identifications we utilized optical spectroscopic information to identify sources with obvious AGN signatures (see criterion 5 below). In the sections below we provide details of each criteria.

1. *X-ray hardness.*—One unique signature of moderately obscured ($N_H \gtrsim 10^{22}$ cm^{-2}) AGN activity is a hard X-ray spectrum. For normal galaxies, the collective emission from X-ray binaries dominates the total 0.5–8 keV power output. On average, these sources have observed power-law X-ray SEDs with spectral slopes of $\Gamma \approx 1.5$–1.7 for LMXBs (e.g., Church & Balucińska-Church 2001; Irwin et al. 2003) and $\Gamma \approx 1$–2 for HMXBs and ULXs (e.g., Sasaki et al. 2003; Liu & Mirabel 2005; Liu et al. 2006); the presence of a significant hot interstellar gas component will steepen the resulting X-ray spectral slope (i.e., produce larger Γ_{eff}). To identify obscured AGNs in our sample effectively, we flagged sources having effective photon indices of $\Gamma_{eff} \lesssim 1$ as AGN candidates. We determined Γ_{eff} using the 2–8 keV to 0.5–2 keV hardness ratio $\Phi_{2-8\,keV}/\Phi_{0.5-2\,keV}$, where Φ is the count rate for each bandpass. A few sources have only 0.5–8 keV detections. Since these sources were not detected in the 0.5–2 keV bandpass, our most sensitive bandpass, there must be a significant contribution from the 2–8 keV bandpass such that $\Phi_{2-8\,keV}/\Phi_{0.5-2\,keV} \gtrsim 1$ ($\Gamma_{eff} \lesssim 0.9$). We therefore classified these sources as AGN candidates. In Figure 5, we show the $\Phi_{2-8\,keV}/\Phi_{0.5-2\,keV}$ hardness ratio versus the logarithm of the 0.5–8 keV flux $\log f_{0.5-8\,keV}$ for the X-ray–detected sources in our main sample. The shaded area highlights the region corresponding to $\Gamma_{eff} \lesssim 1$. Sources that had only upper limits on $\Phi_{2-8\,keV}/\Phi_{0.5-2\,keV}$ that lie in the shaded region were not classified as AGN candidates, while those with lower limits on $\Phi_{2-8\,keV}/\Phi_{0.5-2\,keV}$ that were in the shaded region were flagged as likely AGNs. We note that occasionally an X-ray–luminous ULX that is too close to the nucleus of its host galaxy to be identified as off-nuclear may have $\Gamma_{eff} < 1$ and therefore be classified as an AGN candidate via this criterion; however, since only one identified off-nuclear X-ray source has $\Gamma_{eff} < 1$ (open squares in Fig. 5; n.b., upper limits are not included), we do not expect such rare sources to significantly affect our results. Using criterion 1, we identified a total of 71 obscured AGN candidates.
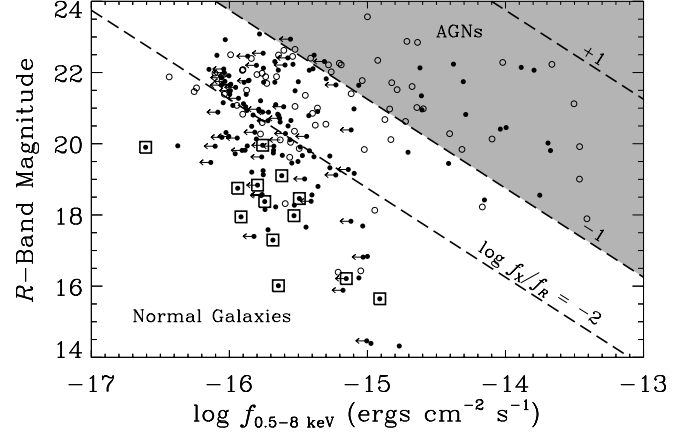
2. *X-ray–to–optical flux ratio.*—Detailed analyses of the X-ray spectra of luminous AGNs in the ≈1 Ms CDF-S show that the intrinsic AGN power-law photon index is relatively steep, $\langle\Gamma\rangle = 1.75 \pm 0.02$ (e.g., Tozzi et al. 2006). Therefore, luminous AGNs having column densities of $N_H \lesssim 10^{22}$ cm^{-2} will often have effective photon indices of $\Gamma_{eff} > 1$ and would not have been classified as potential AGNs by criterion 1. In order to identify luminous AGNs with $N_H \lesssim 10^{22}$ cm^{-2}, we utilized the X-ray–to–optical flux ratio ($f_{0.5-8\,keV}/f_R$) as a discriminator of AGN activity (e.g., Maccacaro et al. 1988; Hornschemeier et al. 2000; Bauer et al. 2004). We identified sources with $\log(f_{0.5-8\,keV}/f_R) > -1$ (see criterion 3 below for justification) as unobscured AGN candidates. In Figure 6, we show the R-band magnitude versus $\log f_{0.5-8\,keV}$ for sources in our main sample; the shaded area shows the region where $\log(f_{0.5-8\,keV}/f_R) > -1$. Sources that were classified as AGN candidates via criterion 1 are denoted with open symbols. In total, 43 X-ray–detected sources satisfied criterion 2, and 16 of these sources were uniquely identified using this criterion (i.e., not identified by criterion 1).

3. *X-ray–to–SFR correlation.*—Taken together, criteria 1 and 2 provide an effective means for identifying AGNs that are affected by large absorption column densities (criterion 1) and those that are notably X-ray overluminous for a given optical luminosity (criterion 2). However, these criteria will still miss moderately luminous unobscured AGNs that have $\log(f_{0.5-8\,keV}/f_R) < -1$ (see, e.g., Peterson et al. 2006). Although an accurate classification for *all* such sources is currently not possible, the situation can be mitigated using the available multiwavelength data. We therefore exploited the correlation between X-ray luminosity L_X and SFR (see § 1) to identify additional AGN candidates in our main sample that have significant X-ray excesses over what is expected based on the L_X-SFR correlation. In order to calculate the rest-frame luminosity ($L_{E_1-E_2}$; where E_1 and E_2 are the photon-energy lower and upper bounds, respectively) of a source having a power-law SED, we used the following equation:

$$L_{E_1-E_2} = 4\pi d_L^2 f_{E_1-E_2}(1+z)^{\Gamma-2}, \qquad (4)$$

where $f_{E_1-E_2}$ is the observed-frame emission in the E_1-E_2 bandpass and d_L is the luminosity distance. Using equation (4) and an adopted photon index of $\Gamma = 2$, we calculated 0.5–8 keV
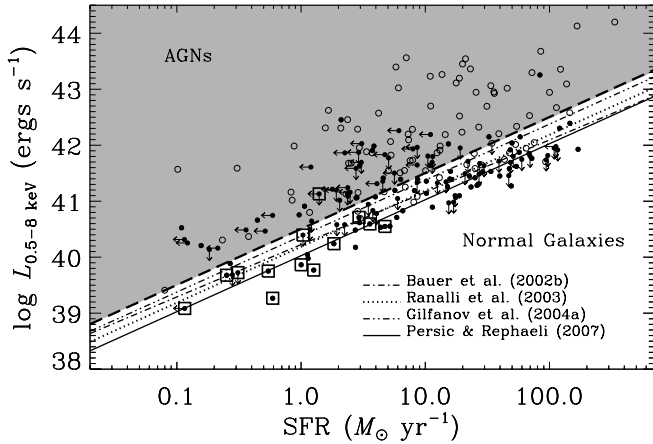
Fig. 7.—Logarithm of the 0.5–8 keV luminosity $L_{0.5-8\,keV}$ vs. SFR for X-ray–detected sources in our sample that have 24 μm counterparts. Open circles represent sources that were classified as AGN candidates via criteria 1 and 2 (see § 4.1 and Figs. 5 and 6), and filled circles represent all other sources; open squares have the same meaning as in Fig. 5. We have shown the X-ray–SFR relations calibrated by Bauer et al. (2002b), Ranalli et al. (2003), Gilfanov et al. (2004a), and PR07; each respective curve has been annotated in the figure. The shaded area above the thick dashed line represents the region where $L_{0.5-8\,keV}$ is 3 times larger than its value predicted by PR07; we classified 0.5–8 keV detections that lie in this region as AGN candidates (see § 4.1, criterion 3).

luminosities for X-ray–detected sources in our sample. In Figure 7, we show the logarithm of the 0.5–8 keV luminosity log $L_{0.5-8\,keV}$ versus SFR (computed following eq. [3]) for galaxies in our main sample that had 24 μm counterparts (see § 3.3). Several estimates of the L_X-SFR correlation have been shown for reference (Bauer et al. 2002a; Ranalli et al. 2003; Gilfanov et al. 2004a; Persic & Rephaeli 2007, hereafter PR07); these correlations have been corrected for differences in X-ray bandpass and SED as well as adopted IMFs. Hereafter, we adopt the L_X-SFR correlation from PR07 for comparisons; however, the use of other L_X-SFR correlations would yield similar results and conclusions. Open squares show the locations of the galaxies hosting off-nuclear sources, which appear to be preferentially located near the L_X-SFR correlation. Open circles indicate sources that were identified as AGN candidates via criteria 1 and 2. Generally, these AGNs have $L_{0.5-8\,keV}$/SFR $\gtrsim$ 3 times that predicted by the PR07 L_X-SFR correlation (*thick dashed line*), which corresponds to a factor of $\gtrsim 2.5$ times the rms scatter of the PR07 L_X-SFR correlation. We therefore classified all sources in this regime (*shaded region*) as AGN candidates. We note that sources having only 0.5–8 keV upper limits were not classified as AGNs. However, sources that were detected in the 0.5–8 keV bandpass that had only upper limits on the SFR were classified as AGN candidates if they were within the shaded region of Figure 7. Using this criterion, we identified 101 potential AGN candidates, of which 33 were unique to criterion 3. For the 124 X-ray–detected sources that were not classified as AGNs, we found that 19 sources ($\approx15\%$) had X-ray spectral properties indicative of AGNs (criterion 1) and only one source ($\approx0.8\%$) had an X-ray–to–optical flux ratio elevated in comparison to normal galaxies (criterion 2).

4. *Infrared and radio properties.*—In addition to the X-ray–detected sources, we also expect there to be additional AGNs that lie below the X-ray detection threshold that are not identified here. In § 3.3, we noted using 48 sources that the SFRs derived from the UV-plus-infrared emission are generally consistent with those derived from radio (1.4 GHz) observations; however, there are a few sources that are significantly scattered (i.e., by more than a factor of 5 times the intrinsic scatter) outside of the

SFR(UV+IR)-SFR(1.4 GHz) correlation. These sources have either (1) excess infrared emission due to reprocessed dust emission from a highly obscured ($N_{\rm H} \gtrsim 10^{24}$ cm^{-2}) moderately luminous (intrinsic $L_X \approx 10^{42}-10^{43}$ ergs s^{-1}) Compton-thick AGN (e.g., Daddi et al. 2007a, 2007b) or (2) an excess of radio emission due to prominent radio-emitting jets (e.g., Snellen & Best 2001). The reasonable agreement between SFR(UV+IR) and SFR(1.4 GHz) suggests that such AGNs are not prevalent in our late-type galaxy sample. Ideally we would also like to explore how UV-corrected SFRs compare to the UV-plus-infrared SFR to search for potential Compton-thick AGNs following the approach used by Daddi et al. (2007a, 2007b) for *BzK* galaxies at $z \gtrsim 2$; however, since our galaxies generally lie at much lower redshifts that the Daddi et al. (2007a, 2007b) sources, we are unable to constrain well UV spectral slopes with our available photometry, which would be required to make dust-corrections to the observed UV SFRs (see § 3.3 for discussion). For our sample of 24 μm–detected galaxies, we identified three radio-excess galaxies with SFR(1.4 GHz)/SFR(UV+IR) > 5 and three IR-luminous galaxies with SFR(1.4 GHz)/SFR(UV+IR) < 1/5. Using these criteria we identified three new AGN candidates, two radio luminous (J33146.6−275735 and J33244.3−275141) and one IR luminous (J33240.0−274214); one of these sources, the radio-luminous source J33244.3−275141, was detected in the 0.5–2 keV and 0.5–8 keV bandpasses.

As an additional test, we utilized IRAC photometry (see § 2.3) to search for infrared power-law sources having near-IR spectral properties characteristic of luminous AGNs (e.g., Alonso-Herrero et al. 2006; Donley et al. 2007). When searching for power-law sources, we adopted the criteria discussed in Donley et al. (2007). We found that no sources in our sample satisfied these criteria, which is consistent with the finding that most IRAC power-law sources reside at $z \gtrsim 1$.

5. *Optical spectroscopy.*—As a final check on our AGN classifications, we searched the optical spectroscopic catalogs available for CDF sources (e.g., Barger et al. 2003; Le Fèvre et al. 2004; Szokoly et al. 2004; Wirth et al. 2004; Vanzella et al. 2005, 2006) to isolate additional luminous AGNs in our sample. In total, we found 15 galaxies in our main sample that were classified as AGNs via optical spectroscopy and all of these sources had been identified as AGN candidates by the previous criteria. We note that the majority of the X-ray–detected AGNs have moderate luminosities (intrinsic $L_X \approx 10^{41}-10^{43}$ ergs s^{-1}) and therefore often have high-excitation AGN emission lines that are too faint with respect to stellar emission to be identified via optical spectroscopy (e.g., Moran et al. 2002). Therefore, it is not surprising that we do not find any additional AGNs using this criterion.

To summarize, in the X-ray band we have detected a total of 225 ($\approx9\%$) late-type galaxies out of the 2568 sources in our main sample. Using the criteria presented above, we classified 121 X-ray–detected sources as AGN candidates (with an additional two X-ray–undetected AGN candidates via criterion 4). The remaining 104 X-ray-detected sources that we do not classify as AGN candidates are considered to be normal late-type galaxies, and we include these galaxies in subsequent X-ray stacking analyses (see details in § 5 below). Thus we use 2447 late-type galaxies in our stacking analyses. In Figure 8, we show log $L_{0.5-8\,keV}$ versus redshift for X-ray–detected sources in our main sample, and in Table 1 we summarize their properties. AGN candidates are denoted with open circles and normal galaxies are plotted with filled circles. We note that the above criteria are not completely sufficient to classify all X-ray–detected sources that are truly AGNs as AGN candidates (see, e.g., Peterson et al. 2006). Such
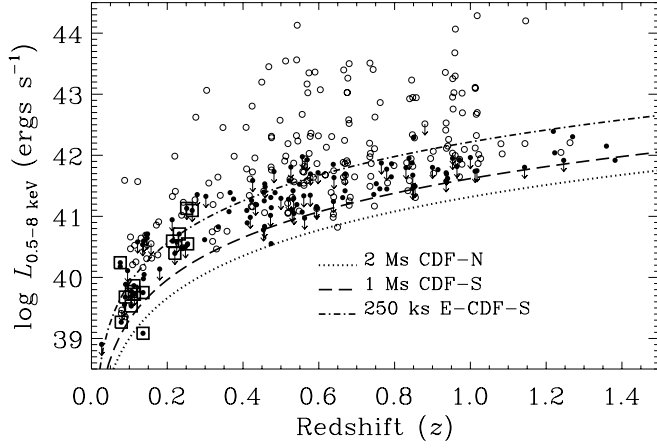
FIG. 8.—Logarithm of the 0.5–8 keV luminosity $L_{0.5-8\,\text{keV}}$ vs. redshift for the 225 X-ray–detected sources in our main sample. Open circles indicate all of the AGN candidates that were isolated using the four criteria outlined in § 4.1, and filled circles represent potential normal galaxies; open squares have the same meaning as in Fig. 5. The estimated 0.5–8 keV detection limits for the ≈2 Ms CDF-N, the ≈1 Ms CDF-S, and the ≈250 ks E-CDF-S have been indicated with dotted, dashed, and dot-dashed curves, respectively.

a misclassification is possible for low-luminosity AGNs that are only detected in the more sensitive 0.5–2 keV bandpass, which have 2–8 keV emission too weak for an accurate classification. In § 5.2, we use the 2–8 keV AGN fraction as a function of X-ray luminosity to argue quantitatively that we do not expect misclassified AGNs (detected only in the 0.5–2 keV bandpass) and low-luminosity AGNs below the X-ray detection limit to have a serious impact on our results.

4.2. X-Ray Stacking Analyses of Normal Late-Type Galaxy Populations

The majority of the normal late-type galaxies that make up our main sample were not detected individually in the X-ray bandpass. In order to study the mean X-ray properties of these sources, we implemented stacking analyses of galaxy populations selected by their physical properties (see § 3). We divided our main sample into subsamples (to be used for stacking) of normal late-type galaxies selected by both physical properties (i.e., B-band luminosity, stellar mass, and star formation rate) and redshifts. In Figure 4, we have highlighted the divisions of our sample with thick gray

rectangles, and for normal late-type galaxies in each region, we used X-ray stacking analyses to constrain average properties.

For each of the subsamples defined above, we performed X-ray stacking in each of the three standard bandpasses (i.e., SB, HB, and FB; see § 1). We expect these bandpasses to sample effectively power-law X-ray emission originating from X-ray binaries (i.e., HMXBs and LMXBs) with a minor contribution from hot interstellar gas in the SB for late-type galaxies at $z \lesssim 0.5$. In our analyses, we used data products presented in Alexander et al. (2003) for the ≈2 Ms CDF-N and ≈1 Ms CDF-S and Lehmer et al. (2005b) for the ≈250 ks E-CDF-S (see footnotes 15 and 16). Our stacking procedure itself was similar to that discussed in § 3 of Steffen et al. (2007). This procedure differs from past stacking analyses (e.g., Lehmer et al. 2007) in how the local X-ray background of each stacked sample is determined, and produces results that are in good agreement with the method discussed in § 2.2 of Lehmer et al. (2007). For completeness, we have outlined this procedure below.

Using a circular aperture with radius $R_{\text{ap}} = 1.5''$, we extracted *Chandra* source-plus-background counts S_i and exposure times T_i (in units of cm^2 s) for each galaxy using images and exposure maps, respectively. For a given source, we used only *Chandra* pointings with aim points (see footnote 12) that were offset from the source position by less than $6.0'$; hereafter, we refer to this maximum offset as the inclusion radius, R_{incl}.[17] Since the *Chandra* PSF increases in size with off-axis angle and degrades the sensitivity for sources that are far off-axis, our choices of R_{ap} and R_{incl} have been chosen to give the maximal stacked signal with the majority of the PSFs being sampled by our stacking aperture (see § 2.2 and Fig. 3 of Lehmer et al. 2007 for justification). We estimate, based on stacked images of $z \approx 0.1-0.3$ optically luminous ($L_B > 2 \times 10^9\, L_{B,\odot}$) late-type galaxies, that ≲10% of the normal galaxy X-ray emission originates outside of our $1.5''$ radius aperture (2.8–6.7 kpc at $z = 0.1-0.3$) for all stacked samples. For galaxies that were within $6.0'$ of more than one of the CDF aim points, we added source counts and exposure times from all appropriate images and exposure maps, respectively; however, there were very few sources in our main sample that met this criterion.

Using background maps (see § 4.2 of Alexander et al. 2003 for the ≈2 Ms CDF-N and ≈1 Ms CDF-S and § 4 of Lehmer et al. 2005b for the ≈250 ks E-CDF-S) and exposure maps, we

---

[17] Note that R_{incl} has the same meaning as it did in Lehmer et al. (2007).

TABLE 1
X-Ray–Detected Late-Type Galaxies: Source Properties

Source Name (J2000.0) (1)	z_{850} (mag) (2)	z (3)	L_B ($\log L_{B,\odot}$) (4)	$M_\star$ ($\log M_\odot$) (5)	SFR ($M_\odot\ \text{yr}^{-1}$) (6)	Survey (7)	$E_{0.5-8\,\text{keV}}$ (ks) (8)	$f_{0.5-8\,\text{keV}}$ ($\log$ ergs cm^{-2} s^{-1}) (9)
J033132.81−280115.9	17.19	0.15^p	10.39	10.49	<5.89	E-CDF-S 03	217	−15.06
J033132.84−280107.5	22.17	0.15^p	8.85	8.44	0.23	E-CDF-S 03	217	−15.45
J033139.20−280222.3	17.06	0.25^p	10.94	11.07	1.40	E-CDF-S 03	206	<−15.15
J033139.97−274157.0	20.14	0.47^s	10.14	10.43	<19.93	E-CDF-S 02	226	−13.46
J033141.79−275635.2	19.58	0.51^p	10.84	10.54	<13.17	E-CDF-S 03	239	−15.02

NOTES.—Col. (1): *Chandra* source name. Col. (2): ACS z_{850}-band magnitude. Col. (3): Redshift estimate. Superscripts "s" and "p" indicate spectroscopic and photometric redshifts, respectively (see § 2 for details). Col. (4): Logarithm of the rest-frame B-band luminosity in units of $L_{B,\odot}$. Col. (5): Logarithm of the stellar mass in units of $M_\odot$. Col. (6): Star formation rate in units of $M_\odot\ \text{yr}^{-1}$. Col. (7): Survey field in which each source was identified. For E-CDF-S identifications, the associated field number (i.e., 01–04) indicates the *Chandra* pointing within which the source was detected (see Lehmer et al. 2005b for details). Col. (8): Effective 0.5–8 keV exposure time (in units of ks). Cols. (9)–(11): Logarithm of the 0.5–8 keV, 0.5–2 keV, and 2–8 keV flux in units of ergs cm^{-2} s^{-1}. Cols. (12)–(14): Logarithm of the 0.5–8 keV, 0.5–2 keV, and 2–8 keV rest-frame luminosity in units of ergs s^{-1}. Col. (15): Effective photon index (Γ_{eff}). Col. (16): Logarithm of the 0.5–8.0 keV to R-band flux ratio. Col. (17): AGN candidate (Y/N)? Col. (18): AGN selection criteria used (i.e., 1–5; see § 4.1 for details). Table 1 is published in its entirety in the electronic edition of the *Astrophysical Journal*. A portion is shown here for guidance regarding its form and content.

measured local backgrounds $B_{i,\mathrm{local}}$ and exposure times $T_{i,\mathrm{local}}$ within a 30 pixel × 30 pixel ($\approx 15'' \times 15''$) square, centered on each source with the $1.5''$ radius circle masked out. Here again, if a source was within $6.0'$ of more than one of the CDF aim points, we summed the local backgrounds and exposure times. We estimated the expected number of background counts in each circular aperture B_i by scaling the background counts within the square by the relative exposure times of the circular aperture and the square (i.e., $B_i = B_{i,\mathrm{local}} \times T_i/T_{i,\mathrm{local}}$). This approach is similar to scaling the background counts in the square by the relative areas of the circular aperture and the square; however, by using exposure times, we are able to account more accurately for spatial variations in pixel sensitivity due to chip gaps, bad pixels, and vignetting. Furthermore, comparisons between this method and the Monte Carlo method used in Lehmer et al. (2007) to compute B_i give excellent agreement and are most convergent for large numbers of Monte Carlo trials.

When stacking galaxy populations, we excluded sources that were (1) classified as AGN candidates (via the criteria outlined in § 4.1), (2) within $10''$ of an unrelated source detected in the X-ray catalogs, (3) within the extent of extended X-ray sources (see Bauer et al. 2002b, § 3.4 of Giacconi et al. 2002, and § 6 of Lehmer et al. 2005b), and (4) located within $3''$ of another late-type galaxy in our main sample. We note that we include X-ray–detected normal galaxies when stacking our samples, since we are interested in the average properties of the normal late-type galaxy population. We tested the effects of including such sources by stacking samples both with and without X-ray–detected sources included, and find similar results for both cases. Typically, the X-ray–detected sources contribute $\approx 10\%$–30% of the counts in the total stacked signal. For each of the subsamples of normal late-type galaxies outlined in Figure 4 (*gray rectangles*), we determined stacked source-plus-background ($S = \sum_i S_i$) and background counts ($B = \sum_i B_i$) to determine net counts ($S - B$). For each stacked sample, we required that the signal-to-noise ratio [S/N $\equiv (S - B)/\sqrt{B}$; where $|S - B| \ll B$ and $B \geq 20$] be greater than or equal to 3 (i.e., $\gtrsim 99.9\%$ confidence) for a detection. For stacked samples without significant detections, $3\,\sigma$ upper limits were placed on the source counts.

We converted the net counts obtained from each stacked sample to absorption-corrected fluxes and rest-frame luminosities using a power-law SED with $\Gamma = 2$. Due to the fact that our $1.5''$ radius stacking aperture encircles only a fraction of the PSF[18] for sources at relatively large off-axis angle, we calculated aperture corrections ξ_i for each stacked source i. Since we are calculating average X-ray counts from the summed emission of many sources of differing backgrounds and exposure times, we used a single, representative exposure-weighted aperture correction, ξ. This factor, which was determined for each stacked sample, was calculated as follows:

$$\xi \equiv \frac{\sum_i \xi_i \times T_i}{T}, \qquad (5)$$

where $T = \sum_i T_i$. The average aperture corrections (ξ) for sources in our main sample were ≈ 1.6, 1.8, and 1.7 for the SB, HB, and FB, respectively. Using our adopted SED, we estimated observed mean X-ray fluxes using the following equation:

$$f_{E_1-E_2} = A_{E_1-E_2} \xi \left(\frac{S - B}{T} \right), \qquad (6)$$

where $A_{E_1-E_2}$ is a bandpass-dependent count-rate–to–flux conversion factor that incorporates both the X-ray SED information as well as Galactic extinction using the column densities listed in § 1. These mean X-ray fluxes were then converted to rest-frame luminosities following equation (4), assuming a photon index of $\Gamma = 2$.

5. RESULTS

5.1. *Stacking Results*

Using the stacking analysis methods discussed in § 4.2, we stacked the late-type galaxy samples presented in Figure 4 (stacked samples are denoted with thick gray rectangles). These samples were selected using L_B, $M_\star$, and SFR, which include 14, 17, and 13 stacked samples (44 total), respectively. In Table 2, we tabulate our X-ray stacking results. We found significant (i.e., S/N $\gtrsim 3$) X-ray detections in the 0.5–2 keV and 0.5–8 keV bandpasses for all stacked samples. In the 2–8 keV bandpass, 15 out of the 44 stacked samples were detected, and these samples generally constitute the most optically luminous and massive galaxies, as well as those galaxies that are most actively forming stars.

In Figure 9, we show the effective photon index (Γ_{eff}) versus the logarithm of the X-ray–to–optical mean flux ratio ($\log f_{0.5-8\,\mathrm{keV}}/f_R$) for our 44 stacked samples (*filled symbols*) that were selected via their observed properties. Effective photon indices were estimated using HB-to-SB count-rate ratios (i.e., $\Phi_{2-8\,\mathrm{keV}}/\Phi_{0.5-2\,\mathrm{keV}}$). All 44 stacked samples have X-ray–to–optical flux ratios and X-ray spectral slopes consistent with normal galaxies (unshaded region in Fig. 9), suggesting that these samples are not heavily contaminated by an underlying population of AGNs.[19] We find a median logarithm of the X-ray–to–optical flux ratio of $\log f_{0.5-8\,\mathrm{keV}}/f_R = -2.53$ (*vertical dotted line*), and for samples that were detected in both the HB and SB, the median effective photon index is $\Gamma_{\mathrm{eff}}^{\mathrm{median}} = 1.47$ (*horizontal dotted line*). These values are characteristic of galaxies dominated by X-ray binary populations.

In Figure 10, we show the logarithm of the ratio of the 0.5–8 keV luminosity (hereafter, L_X) to each physical property (i.e., $\log L_X/L_B$, $\log L_X/M_\star$, and $\log L_X$/SFR) versus redshift for our samples. Each relevant quantity for the MW and local galaxies M101, M82, and NGC 3256 have been shown for comparison. We adopt 6.6×10^{39} ergs s^{-1} as the approximate X-ray luminosity of the MW (Grimm et al. 2002). For the local galaxies, we utilized the X-ray luminosities from Shapley et al. (2001; hereafter S01) for M101 ($L_X = 1.6 \times 10^{40}$ ergs s^{-1}) and M82 ($L_X = 4.6 \times 10^{40}$ ergs s^{-1}) and Lira et al. (2002) for NGC 3256 ($L_X = 4.0 \times 10^{41}$ ergs s^{-1}). We have corrected the X-ray luminosities to be consistent with our use of the 0.5–8 keV bandpass and our choice of $\Gamma = 2$.

For the purpose of comparing our results to those for nearby late-type galaxy populations, we made use of the S01 sample of 183 normal local ($D \lesssim 100$ Mpc) spiral and irregular galaxies. These galaxies were observed in the 0.2–4 keV band using the *Einstein* IPC and HRI (Fabbiano et al. 1992) and AGNs, with luminous X-ray emission or spectral signatures indicative of AGN activity, have been excised from the sample. To avoid the inclusion of early-type S0 galaxies, we chose to utilize 139 normal late-type galaxies from the S01 sample with morphological types $T > 2$ (Sa–Irr Hubble types).

---

[18] At off-axis angles $\theta \approx 3'$, our $1.5''$ radius circular aperture contains an encircled-energy fraction of $\approx 100\%$, 80%, and 100% for the SB, HB, and FB, respectively; however at $\theta \approx 6'$, this fraction decreases to $\approx 30\%$, 25%, and 25%, respectively.

[19] We note that two of our samples have spectral slopes that are near our chosen division between normal galaxies and AGNs ($\Gamma_{\mathrm{eff}} \sim 1$). These samples have $\log L_B = 10$–10.5 and $\log M_\star = 9.5$–10.1 and lie at $z \approx 0.66$, a redshift where large-scale sheets of galaxies and AGNs have been isolated previously in the CDF-S (e.g., Gilli et al. 2003). These galaxies have spectral slopes that are either statistically scattered toward $\Gamma_{\mathrm{eff}} = 1$ (see characteristic error bar in Fig. 9) or may have some nonnegligible contribution from heavily obscured AGNs.

SELECTION TYPE (1)	z_{mean} (2)	N_{gal} (3)	N_{det} (4)	NET SOURCE COUNTS ($S - B$) 0.5–8 keV (5)	0.5–2 keV (6)	2–8 keV (7)	SIGNAL-TO-NOISE RATIO 0.5–8 keV (8)	0.5–2 keV (9)	2–8 keV (10)
$\log L_B/L_{B,\odot} = 9.5–10.0$	0.23 ± 0.06	120	9	213.3	158.7	54.9	8.6	9.6	3.0
	0.46 ± 0.06	363	1	176.7	152.6	25.3	4.8	6.8	0.9
$\log L_B/L_{B,\odot} = 10.0–10.5$	0.24 ± 0.02	28	2	66.9	46.5	20.2	5.2	5.3	2.1
	0.33 ± 0.03	33	3	82.9	68.5	14.9	5.9	6.7	1.5
	0.41 ± 0.03	67	7	204.2	144.7	59.8	9.3	9.7	3.8
	0.50 ± 0.02	158	6	347.5	240.0	109.1	10.7	11.3	4.4
	0.57 ± 0.02	100	3	128.0	109.0	18.7	6.0	7.5	1.2
	0.67 ± 0.02	71	2	154.1	93.5	60.6	6.3	6.1	3.2
	0.75 ± 0.02	62	2	156.3	107.4	48.8	6.4	6.9	2.6
	0.84 ± 0.02	57	3	105.9	64.8	41.2	4.4	4.5	2.2

NOTES.—Col. (1): Physical property (i.e., L_B, $M_\star$, and SFR) used to select the stacked sample. Col. (2): Mean redshift (z_{mean}) and 1 σ standard deviation. Col. (3): Number of galaxies stacked (N_{gal}). Col. (4): Number of X-ray–detected normal galaxies stacked. Cols. (5)–(7): Net source counts ($S - B$) for the 0.5–8 keV, 0.5–2 keV, and 2–8 keV bandpasses. Cols. (8)–(10): Signal-to-noise ratio for the 0.5–8 keV, 0.5–2 keV, and 2–8 keV bandpasses. Cols. (11)–(13): Logarithm of the mean 0.5–8 keV, 0.5–2 keV, and 2–8 keV flux in units of ergs cm^{-2} s^{-1}. Col. (14)–(16): Fraction of the mean 0.5–8 keV, 0.5–2 keV, and 2–8 keV flux originating from the X-ray–undetected galaxies. Cols. (17)–(19): Logarithm of the mean 0.5–8 keV, 0.5–2 keV, and 2–8 keV rest-frame luminosity. Col. (20): Mean effective photon index (Γ_{eff}). Col. (21): Logarithm of the 0.5–8.0 keV to R-band flux ratio. Cols. (22)–(24): Mean values of L_B, $M_\star$, and SFR for samples selected by L_B, $M_\star$, and SFR, respectively. Cols. (25)–(27): Logarithm of the ratios L_X/L_B (ergs s^{-1} $L_{B,\odot}^{-1}$), $L_X/M_\star$ (ergs s^{-1} $M_\odot^{-1}$), and L_X/SFR [ergs s^{-1} $(M_\odot$ yr$^{-1})^{-1}$] for samples selected by L_B, $M_\star$, and SFR, respectively. Cols. (28)–(30): Estimated fraction of the mean 0.5–8 keV, 0.5–2 keV, and 2–8 keV stacked emission originating from undetected AGNs. Table 2 is published in its entirety in the electronic edition of the *Astrophysical Journal*. A portion is shown here for guidance regarding its form and content.

The S01 sample covers ranges of L_B and $M_\star$ that are well-matched to our main sample and are representative of late-type galaxies in the local universe. In order to compute mean X-ray luminosities for samples that were directly comparable with our results, we divided the S01 sample into the same intervals of L_B and $M_\star$ that were used for our main sample (see Figs. 4a and 4b). Since several of the S01 galaxies had only X-ray upper limits available, we computed mean X-ray luminosities and errors using the Kaplan-Meier estimator available through the Astronomy SURVival Analysis software package (ASURV rev. 1.2; Isobe &
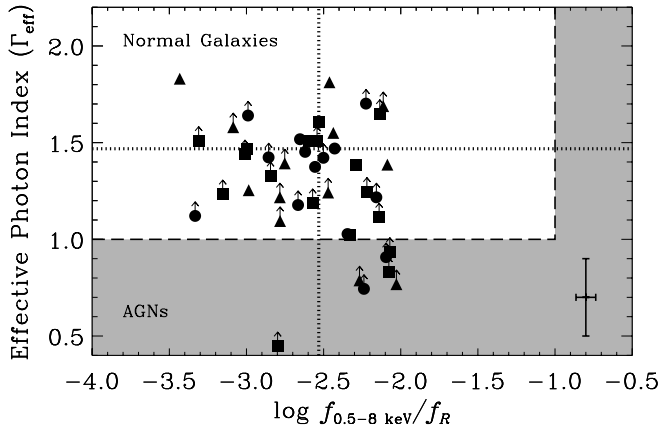

FIG. 9.—Effective photon index (Γ_{eff}) vs. the logarithm of the X-ray–to–optical flux ratio ($\log f_{0.5–8 \text{ keV}}/f_R$) for 44 stacked samples selected via observed properties: L_B (*filled circles*), $M_\star$ (*filled squares*), and SFR (*filled triangles*). The characteristic mean error bar for each quantity is given in the lower right-hand corner. The median logarithm of the X-ray–to–optical flux ratio is indicated with a vertical dotted line ($\log f_{0.5–8 \text{ keV}}/f_R = -2.53$). The median effective photon index for the samples that were detected in both the SB and HB is indicated with a horizontal dotted line ($\Gamma_{eff}^{median} = 1.47$). We note that all of the stacked samples with both SB and HB detections have $\Gamma_{eff} > 1$, consistent with normal galaxies. For the several stacked samples that have only SB detections, we have indicated lower limits on Γ_{eff}. The shaded regions and corresponding boundaries (*dashed lines*) represent areas where X-ray–detected sources were classified as AGN candidates (for details, see discussion of criteria 1 and 2 in § 4.1); note that additional criteria were used to identify potential AGNs when generating our samples of normal late-type galaxies (see criteria 3–5 in § 4.1).
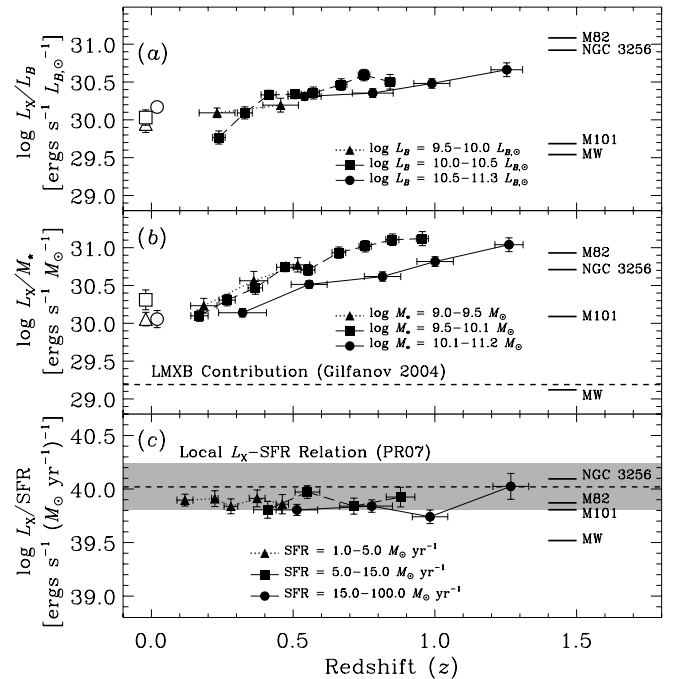

FIG. 10.—Logarithm of (a) the X-ray–to–B band mean luminosity ratio ($\log L_X/L_B$), (b) the X-ray–to–stellar mass mean ratio ($\log L_X/M_\star$), and (c) the X-ray–to–star formation rate mean ratio ($\log L_X/SFR$) vs. redshift (*filled symbols and curves*) for stacked normal late-type galaxy samples selected by L_B (Fig. 4a), $M_\star$ (Fig. 4b), and SFR (Fig. 4c), respectively. For comparison, in each panel we have indicated the properties of the MW and local galaxies M101, M82, and NGC 3256. Quoted X-ray luminosities correspond to the 0.5–8 keV bandpass and were calculated following the methods described in § 4.2, assuming a power-law SED with photon index of $\Gamma = 2$. Symbols and curves correspond to unique ranges of L_B, $M_\star$, and SFR, which are annotated in each respective figure. For reference, in (a) and (b) we have plotted the corresponding values of $\log L_X/L_B$ and $\log L_X/M_\star$, respectively, for normal late-type galaxies in the local universe (*open symbols*) using the S01 sample. In (b) we show the expected LMXB contribution based on Gilfanov (2004; *dashed line*). Finally, in (c) we show the local L_X-SFR relation and its dispersion (*dashed line with shading*) derived by PR07 and corrected for our choice of IMF and $\Gamma = 2$. We note that roughly all of our data points in (c) lie $\approx 0.1–0.2$ dex below the PR07 relation, which is likely due to systematic differences in how L_X and SFR were determined between studies.

Feigelson 1990; LaValley et al. 1992); the Kaplan-Meier estimator handles censored data sets appropriately. When computing these mean X-ray luminosities, we filtered the S01 samples appropriately into distance intervals to avoid the Malmquist bias. In Figures 10a and 10b, we show the corresponding values of $\log L_X/L_B$ and $\log L_X/M_\star$, respectively, for the S01 sample with open symbols. By contrast, the SFRs of the local sample are generally too low ($\lesssim 1$–$10\ M_\odot\ \mathrm{yr}^{-1}$) to provide a meaningful comparison with our distant 24 μm–detected sources. This is due to the strong positive evolution of the star formation rate density with redshift (see § 1), which makes SFRs that are common for galaxies in our sample ($\gtrsim 1$–$10\ M_\odot\ \mathrm{yr}^{-1}$) comparatively rare at $z = 0$.

From Figures 10a and 10b, it is apparent that there is significant positive redshift evolution in $\log L_X/L_B$ and $\log L_X/M_\star$ over the redshift range of $z \approx 0$–1.4. For each of the six total selection ranges of L_B and $M_\star$, the redshift progression of X-ray luminosities is inconsistent with a constant at the >99.9% confidence level. For the most optically luminous [$L_B = (3$–$20) \times 10^{10}\ L_{B,\odot}$] and massive [$M_\star = (1$–$20) \times 10^{10}\ M_\odot$] late-type galaxies at $z = 1.4$, L_X/L_B, and $L_X/M_\star$ are measured to be larger than the local values of S01 by factors of 3.1 ± 0.7 and 9.6 ± 3.1, respectively. Such values are consistent with the $\approx (1 + z)^{1.5-3}$ evolution of L_X^* found for the normal late-type galaxy population, which has been constrained using largely the most optically luminous and massive galaxies (Ptak et al. 2007; Tzanavaris & Georgantopoulos 2008).

The above results confirm the increase in L_X/L_B with redshift found by H02. In past studies, L_X/L_B has been used as a proxy for star formation activity (e.g., Ptak et al. 2001; H02; Lehmer et al. 2005a), despite the fact that L_B is likely to be somewhat sensitive to SFR (see discussion in § 3.1). As discussed in § 1, L_X has been shown to be strongly correlated with galaxy SFR. Correlation studies of spiral galaxies in the local universe have also found strong correlations between L_X and L_B such that $L_X \propto L_B^{1.5}$ (S01; Fabbiano & Shapley 2002). The nonlinear relationship between X-ray and B-band emission is thought to be due to the increase in dust obscuration with star formation activity, which attenuates light from the B-band more effectively than it does in the X-ray band. Using our sample of 47 normal late-type galaxies with both X-ray and 24 μm detections, we found that L_X/L_B was positively correlated with the UV dust-extinction measure $(L_{IR} + L_{UV})/L_{UV}$ (Kendall's $\tau = 0.44$; $\gtrsim 99.99\%$ confidence level), thus providing support for this hypothesis. Furthermore, it has been shown that L_X/L_B is correlated with $L_{60\mu m}/L_{100\mu m}$, suggesting that more intense X-ray emission is associated with hotter IR colors, which is indicative of intense obscured star formation activity. Therefore, the increase in L_X/L_B with redshift (see Fig. 10a) observed for our galaxies is likely due to an increase in their star formation activity.

Upon comparing L_B with $M_\star$ and SFR for our galaxies, we find that L_B is well correlated with both $M_\star$ (Kendall's $\tau = 0.69$) and SFR ($\tau = 0.58$); however, the scatter in the L_B-$M_\star$ relation is significantly smaller than it is for the L_B-SFR relation (≈ 0.2 dex vs. ≈ 0.4 dex, respectively), implying that L_B traces more effectively $M_\star$ rather than SFR. It is therefore not surprising that we see similar redshift evolution of $L_X/M_\star$ and L_X/L_B.

In Figure 10b, we show the estimated LMXB contribution to $\log L_X/M_\star$ (dashed line) based on Table 5 of Gilfanov (2004). This value is ≈ 5–10 times lower than all mean values of $L_X/M_\star$, suggesting that on average LMXBs play a fairly small role in the X-ray emission from our stacked samples. Furthermore, late-type galaxies in the local universe with similar stellar masses are often found to have HMXB emission that is ≈ 2–10 times more luminous than that expected from LMXBs (see open symbols in

Fig. 10b and Fig. 3 of Gilfanov et al. 2004b). For galaxy samples selected via SFR, we find no evidence for significant evolution in $\log L_X$/SFR (Fig. 10c). We note that if the majority of the X-ray flux from our stacked samples originated from X-ray–detected sources, then the AGN selection criteria 3 and 4 from § 4.1 may potentially bias these results. However, we find that the more populous and unbiased X-ray–undetected source populations dominate the stacked 0.5–8 keV signals at the $\gtrsim 80\%$ level (see col. [14] of Table 2). For each of the three ranges of SFR, $\log L_X$/SFR is consistent with a constant value and has a best-fit ratio of $\log L_X$/SFR $= 39.87 \pm 0.07$ ($\chi^2 = 13.1$ for 12 degrees of freedom). These results suggest that the contribution from LMXBs is small and that the integrated X-ray emission from our late-type galaxies is dominated by HMXBs. This implies that the evolution of our late-type galaxy samples is likely due to changes in star formation activity.

Since the X-ray emission from our late-type galaxies is dominated by star formation processes, we note that our $M_\star$-selected stacking results provide a relatively unobscured measure of the star formation activity per unit stellar mass (i.e., the SSFR; see Fig. 10b). We find that at $z \approx 1$ the X-ray emission per unit stellar mass is a factor of ≈ 2–3 larger for galaxies with $M_\star = (3$–$10) \times 10^9\ M_\odot$ versus that observed for galaxies with $M_\star = (1$–$20) \times 10^{10}\ M_\odot$. At $z \approx 1$, we find that $L_X/M_\star$ is larger than its local value (S01) by factors of 6.4 ± 2.2 and 5.8 ± 1.6 for late-type galaxies with $M_\star = (3$–$10) \times 10^9\ M_\odot$ and $M_\star = (1$–$20) \times 10^{10}\ M_\odot$, respectively. These results are broadly consistent with observed differences in the mean SSFRs found by Zheng et al. (2007) for $z \approx 1$ galaxies of comparable stellar masses, and imply that the lower mass galaxies are undergoing more significant stellar mass growth over $z \approx 0$–1 than more massive galaxies.

In order to quantify the dependences of the X-ray luminosity on redshift and physical properties, we performed multivariate parametric fitting to our stacked data. For each galaxy sample selected via L_B, $M_\star$, and SFR, we investigated the redshift evolution of the X-ray luminosity. For this analysis, we fit our data to a power-law parametric form:

$$\log L_X(f_{phys},\ z) = A + B \log f_{phys} + C \log (1 + z), \quad (7)$$

where f_{phys} is a place holder for each of the three physical properties (L_B, $M_\star$, and SFR) used for our sample selections, and A, B, and C are fitting constants. For each sample, we utilized our X-ray stacking results, equation (7), and χ^2 fitting to estimate the constants A, B, and C. For our adopted three-component model, we constrained A, B, and C using 90% confidence errors ($\Delta\chi^2 = 2.7$). The S01 local data points were not used for these fits due to differences in galaxy selection, instrument calibration, and AGN identification.

In Table 3, we tabulate our constraints on χ^2, A, B, and C for these fits. We find that this particular choice (i.e., eq. [7]) of parameterization does not provide acceptable fits for galaxy samples selected via L_B and $M_\star$. However, for galaxy samples selected via SFR, we find a good fit for this parameterization ($\chi^2 = 9.72$ for 10 degrees of freedom). We constrain the evolution of $\log L_X$/SFR to be independent of or at most weakly dependent on redshift [$\propto (1 + z)^{0.32 \pm 0.88}$].

Based on radio observations of distant star-forming galaxies with SFR ≈ 3–$300\ M_\odot\ \mathrm{yr}^{-1}$ in the CDF-N and CDF-S, Barger et al. (2007) reported that the X-ray upper limits for X-ray–undetected sources were below the level expected from the L_X-SFR correlation, thus suggesting that the correlation may not hold in the high-redshift universe. However, our stacking

TABLE 3
PARAMETRIC FITTING RESULTS FOR STACKED SAMPLES

f_{phys} (1)	ν (2)	χ^2 (3)	A (4)	B (5)	C (6)
L_B................	11	25.37	31.34 ± 1.23	0.85 ± 0.13	2.91 ± 0.61
$M_\star$................	14	25.73	33.97 ± 0.87	0.58 ± 0.07	4.48 ± 0.37
SFR	10	9.72	39.91 ± 0.06	0.89 ± 0.11	0.32 ± 0.88

NOTES.—This table contains basic fitting parameters for χ^2 fits to our X-ray stacking results. For each sample, selected by physical property f_{phys}, we performed parametric fits for the mean 0.5–8 keV luminosity L_X following $\log L_X = A + B \log f_{phys} + C \log (1 + z)$. Col. (1): Physical parameter f_{phys} used in fitting our stacking results. Col. (2): Number of degrees of freedom used in each fit. Col. (3): Minimum χ^2 value for each fit. Cols. (4)–(6): Best-fit values of A, B, and C with errors (90% confidence). For further details, see § 5.1.

results suggest that the L_X-SFR correlation *does* in fact hold for average galaxies with SFR = 1–5 $M_\odot$ yr^{-1} (SFR = 15–100 $M_\odot$ yr^{-1}) out to $z \approx 0.5$ ($z \approx 1.4$).

For illustrative purposes we have created Figure 11, which shows log SFR versus log L_X for normal star-forming galaxies selected from several different sources including X-ray–detected galaxies from our main sample (*filled gray circles and limits*), stacked galaxies from this study (*filled black symbols*), local galaxies from PR07 (*open circles*), local ultraluminous infrared galaxies from PR07 (ULIRGs; *open squares*), and stacked $z \sim 3$ Lyman break galaxies (LBGs; *stars*; see § 6 for details). For all data used in this plot, we have normalized SFRs appropriately to be consistent with our adopted Kroupa (2001) IMF and have adjusted X-ray luminosities to correspond to the 0.5–8 keV band using a $\Gamma = 2$ power-law SED. The best-fit L_X-SFR correlations for local galaxies from PR07 (*solid curve*) and $z = 0$–1.4 late-type galaxies from this study (log L_X/SFR = 39.87; *dotted curve*) have been shown for reference. For comparison, we have shown the SFRs for the MW and local galaxies M101, M82, and NGC 3256.

5.2. AGN Contribution to Stacked Signals

In this section we estimate the contribution to our stacked signals from contaminating AGNs that have X-ray luminosities below our X-ray detection limit. This analysis is similar in nature to that in §§ 3.1 and 3.2.2 of Lehmer et al. (2007), which was performed for early-type galaxies. We implement the observed cumulative AGN fraction f_C: the fraction of galaxies harboring an AGN with 2–8 keV luminosity of $L_{2-8\,keV}$ or greater. Hereafter, we compute f_C by taking the number of candidate AGNs in a particular galaxy sample with a 2–8 keV luminosity of $L_{2-8\,keV}$ or greater and dividing it by the number of galaxies in which we could have detected an AGN with luminosity $L_{2-8\,keV}$. The latter number is computed by considering the redshift of each galaxy and its corresponding sensitivity limit, as obtained from spatially varying sensitivity maps (see § 4.2 of Alexander et al. 2003 and § 4 of Lehmer et al. 2005b); these sensitivity maps were calibrated empirically using sources detected by wavdetect at a false-positive probability threshold of 1×10^{-5}.

The quantity f_C is not only a function of $L_{2-8\,keV}$, but is also dependent on the selection of the galaxy sample considered: in our case redshift and the physical property f_{phys} (i.e., L_B, $M_\star$, and SFR) of the galaxy population may plausibly play a role in f_C. In our analyses, we assume that each of the respective dependencies (i.e., $L_{2-8\,keV}$, z, and f_{phys}) are independent of each other, such that $f_C \propto g_L(L_{2-8\,keV}) \times g_z(z) \times g_p(f_{phys})$, where g_L, g_z, and g_p represents the functional dependence of the cumulative AGN fraction for each indicated variable $L_{2-8\,keV}$, z, and f_{phys}, respectively. We made use of the 2–8 keV bandpass because of
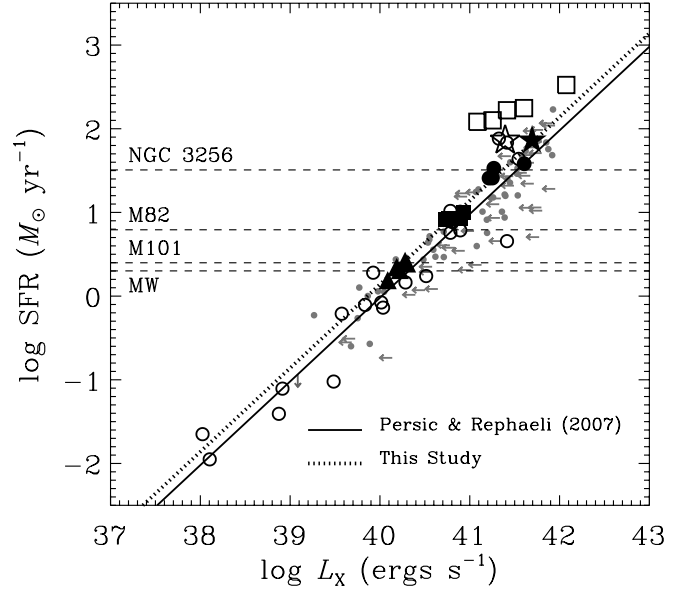

FIG. 11.—Logarithm of the star formation rate log SFR vs. the logarithm of the X-ray luminosity (log L_X) for normal late-type galaxies. X-ray–detected sources from our main sample are indicated as small gray dots. Sources that were not detected in the 0.5–8 keV bandpass but were detected in either the 0.5–2 keV or 2–8 keV bandpasses are shown as upper limits. Results from our X-ray stacking analyses of late-type galaxies selected via observed SFR are shown as large filled circles, squares, and triangles, which have the same meaning as in Fig. 10c; $z \sim 3$ LBGs that were both uncorrected and corrected for AGN contamination have been plotted as a filled star and open star, respectively. For comparison, we show the local galaxy sample from PR07, which includes normal late-type galaxies (*open circles*) and ultraluminous infrared galaxies (ULIRGs; *open squares*); the best-fit PR07 relation is shown as a solid curve. The SFRs for the MW and local galaxies M101, M82, and NGC 3256 are indicated (*horizontal dashed lines*).

its ability to probe relatively unattenuated X-ray emission in a regime of the X-ray spectrum where we expect there to be minimal emission from normal galaxies (see also criterion 1 of § 4.1 for further details). In total 62 ($\approx 51\%$) of our 121 X-ray–detected AGN candidates had 2–8 keV detections; we use these AGNs in our AGN fraction analyses.

We began constructing f_C by estimating the shape of $g_L(L_{2-8\,keV})$ using late-type galaxies with $z = 0$–1 and $L_B \gtrsim 2 \times 10^{10}\, L_{B,\odot}$, an optical luminosity regime where we have a relatively large number of sources and are sufficiently complete out to $z = 1$ (see Fig. 4a). We split this sample into two subsets about $z = 0.6$, to test whether there is substantial evolution in the shape and normalization of $g_L(L_{2-8\,keV})$ over this redshift range. In Figure 12, we show $g_L(L_{2-8\,keV})$ for galaxies in the redshift ranges $z \lesssim 0.6$ ($z_{median} = 0.51$; *filled circles*) and $z = 0.6$–1 ($z_{median} = 0.84$; *open triangles*). From Figure 12, we see that the overall shape and normalization of $g_L(L_{2-8\,keV})$ for late-type galaxies with $L_B \gtrsim 2 \times 10^{10}\, L_{B,\odot}$ is similar for galaxies at $z_{median} = 0.51$ and $z_{median} = 0.84$. We fit the shape of $g_L(L_{2-8\,keV})$ using least-squares fitting of the 2–8 keV luminosity dependent cumulative AGN fraction using all galaxies from $z = 0$ to 1 with $L_B \gtrsim 2 \times 10^{10}\, L_{B,\odot}$. For these fits, we found that the data were well fit by an exponential function, which we parameterized as $\log g_L(L_{2-8\,keV}) \propto a \exp [-b(\log L_{2-8\,keV} - 39)^2]$, where a and b are fitting constants. By construction, this function is only valid for $\log L_{2-8\,keV} > 39$, which is ≈ 1–2 orders of magnitude less luminous than a typical stacked X-ray luminosity of our late-type galaxy samples (see Table 2 and Fig. 10). We find best-fit values of $a = -0.8$ and $b = -0.05$; in Figure 12 (*thick black curve*), we show our best-fit relation for $g_L(L_{2-8\,keV})$.
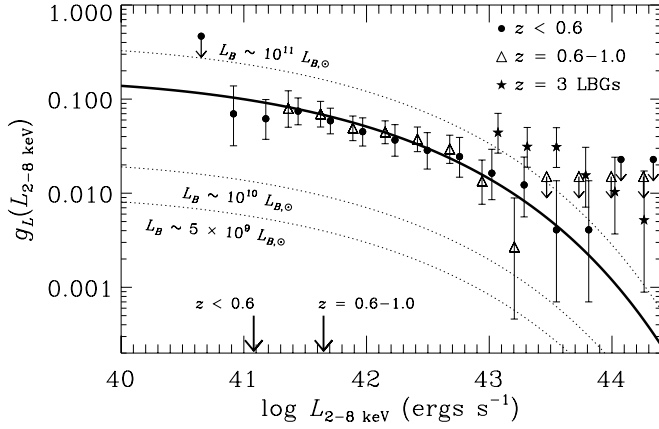
FIG. 12.—Cumulative X-ray luminosity dependent AGN fraction $g_L(L_{2-8\,\mathrm{keV}})$ vs. $L_{2-8\,\mathrm{keV}}$ for late-type galaxies with $L_B \gtrsim 2 \times 10^{10}\,L_{B,\odot}$ at $z \lesssim 0.6$ (*filled circles*) and $z \approx 0.6–1$ (*open triangles*). For reference, we have indicated the corresponding AGN fraction for Lyman break galaxies at $z \sim 3$ (*filled stars*; see § 5 for further details). We have indicated the median X-ray detection limit for galaxies in each redshift range (*downward-pointing arrows along the x-axis*). The solid curve represents the best-fit relation for $g_L(L_{2-8\,\mathrm{keV}})$, which was fit using all late-type galaxies with $z \approx 0–1$ and $L_B \gtrsim 2 \times 10^{10}\,L_{B,\odot}$ in our main sample. For reference, we have shown the estimated AGN fraction for galaxies with $L_B \approx 5 \times 10^9$, 10^{10}, and $10^{11}\,L_{B,\odot}$ (*dotted curves*; see § 5.2 for further details).

We constrained further the redshift evolution of f_C [i.e., the shape of $g_z(z)$] by dividing our main late-type galaxy sample into five nearly independent redshift bins (with $z = 0.1–0.8$) and calculating f_C for fixed ranges of $L_{2-8\,\mathrm{keV}}$ and f_{phys}. In Figure 13, we show $g_z(z)$ as a function of redshift for late-type galaxies with $L_{2-8\,\mathrm{keV}} \gtrsim 10^{41.5}$ ergs s^{-1} and $L_B \gtrsim 10^{10}\,L_{B,\odot}$, the approximate completeness limit at $z \approx 0.8$ (see Fig. 4a). Using these data and χ^2 fitting [assuming a $(1+z)^n$ dependence], we constrained the redshift evolution of $g_z(z)$ to be proportional to $(1+z)^{0.15\pm0.97}$; similar results were found for different ranges of $L_{2-8\,\mathrm{keV}}$ and L_B. This result differs from that observed for early-type galaxies, where the AGN fraction and mean AGN emission has been found to evolve as $\approx(1+z)^3$ (e.g., Brand et al. 2005; Lehmer et al. 2007).[20] We therefore conclude that there is little redshift evolution in the late-type galaxy AGN fraction over the redshift range $z = 0.1–0.8$, and hereafter we assume that $g_z(z)$ remains roughly constant out to $z = 1.4$.

To constrain the overall dependence of f_C on f_{phys} [i.e., $g_p(f_{\mathrm{phys}})$], we calculated the cumulative AGN fractions for late-type galaxy samples with f_{phys} by holding the ranges of $L_{2-8\,\mathrm{keV}}$ and z fixed and varying f_{phys}. In Figure 14, we show $g_p(f_{\mathrm{phys}})$ versus $\log L_B$ (Fig. 14, *left*), $\log M_\star$ (Fig. 14, *middle*), and $\log$ SFR (Fig. 14, *right*) for $L_{2-8\,\mathrm{keV}} \gtrsim 10^{41.5}$ ergs s^{-1} at $z \lesssim 0.6$ (*dashed curves*) and $z = 0.6–1$ (*dotted curves*). We calculated $g_p(f_{\mathrm{phys}})$ for intervals of f_{phys} where we are approximately complete at $z = 0.6$ (for the $z \lesssim 0.6$ interval) and $z = 1$ (for the $z = 0.6–1$ interval; see Fig. 4). For each sample, we again utilized least-squares fitting to approximate the f_{phys} dependence of $g_p(f_{\mathrm{phys}})$. These fits were performed using all data over the redshift range $z = 0–1$ assuming a functional dependence of $\log g_p(f_{\mathrm{phys}}) \propto c \log f_{\mathrm{phys}}$. In each panel of Figure 14, we show the best-fit solutions for $g_p(f_{\mathrm{phys}})$ with the gray lines. We find
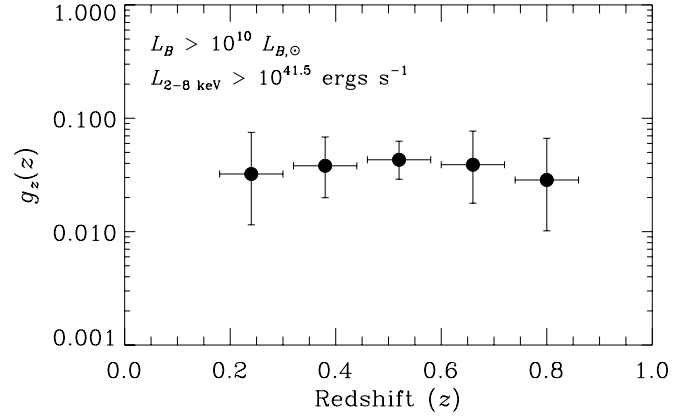

FIG. 13.—Cumulative redshift-dependent AGN fraction $g_z(z)$ vs. redshift for late-type galaxy samples with $L_B \gtrsim 10^{10}\,L_{B,\odot}$ and $L_{2-8\,\mathrm{keV}} \gtrsim 10^{41.5}$ ergs s^{-1}. We find no significant evolution of $g_z(z)$ over the redshift range $z \approx 0.1–0.8$.

that the AGN fraction is strongly dependent on L_B (Fig. 14, *left*) and $M_\star$ (Fig. 14, *middle*), such that more optically luminous and massive galaxies have larger AGN fractions; this result is consistent with other studies of the AGN host galaxies (e.g., Kauffmann et al. 2003b; Nandra et al. 2007; Silverman et al. 2008). Also, the AGN fraction seems to be mildly dependent on the galaxy SFR; however, this is likely due to the fact that the SFR is larger on average for more massive galaxies.

Based on the above estimates of the shapes of $g_L(L_{2-8\,\mathrm{keV}})$, $g_z(z)$, and $g_p(f_{\mathrm{phys}})$, we approximated empirically f_C for each choice of f_{phys} following

$$\log f_C = \log g_0 + a \exp\left[-b(\log L_{2-8\,\mathrm{keV}} - 39)^2\right] + c \log f_{\mathrm{phys}}, \tag{8}$$

where g_0 represents the normalization of each relation based on the value of f_C at $L_{2-8\,\mathrm{keV}} > 10^{41.5}$ ergs s^{-1} and $L_B = 10^{10}\,L_{B,\odot}$, $M_\star = 10^{10}\,M_\odot$, and SFR = 2 $M_\odot$ yr^{-1}, for galaxy samples selected via L_B, $M_\star$, and SFR, respectively. We note that only g_0 and c are dependent on our choice of f_{phys}; we find for the set of physical parameters $f_{\mathrm{phys}} = [L_B, M_\star, \mathrm{SFR}]$ that $g_0 = [6.1 \times 10^{-14}, 8.2 \times 10^{-8}, 0.20]$ and $c = [1.2, 0.67, 0.66]$. For reference, in Figure 12 we have shown curves of f_C for $L_B = 5 \times 10^9$, 10^{10}, and $10^{11}\,L_{B,\odot}$ (*dotted curves*).

To estimate the AGN contamination expected for each of our stacked samples presented in § 5.1, we followed closely the procedure in § 3.2.2 of Lehmer et al. (2007). For completeness, we outline this procedure below.

For each stacked sample, we used equation (8) to compute cumulative AGN fractions f_C. In Figure 15a, we show f_C for two of our L_B-selected samples: $z \approx 0.2$ galaxies with $L_B = 10^{9.5}–10^{10}\,L_{B,\odot}$ (*dashed curve*) and $z \approx 1.3$ galaxies with $L_B = 10^{10.5}–10^{11.3}\,L_{B,\odot}$ (*solid curve*). We then converted f_C for each sample to a differential AGN fraction f_D (i.e., the 2–8 keV luminosity dependent fraction of galaxies harboring AGNs within discrete X-ray luminosity bins of width $\Delta \log L_{2-8\,\mathrm{keV}} = 0.5$; see Fig. 15b). For each sample, we calculated the 2–8 keV luminosity dependent fraction of galaxies that were below our $L_{2-8\,\mathrm{keV}}$ detection limit f_B (Fig. 15c). We then multiplied f_D and f_B to estimate the 2–8 keV luminosity dependent fraction of galaxies harboring an AGN that was undetected in the *Chandra* exposures f_U (i.e., $f_U = f_D \times f_B$; see Fig. 15d); these AGNs would *not* have been removed for our stacking analyses. Finally, we approximated the total 2–8 keV AGN contamination

---

[20] We note that the lack of evolution of the AGN fraction does *not* necessarily imply that the optically luminous (i.e., $L_B \gtrsim 10^{10}\,L_{B,\odot}$) late-type galaxy AGN number density is constant over $z \approx 0–1$. For example, L_B^* has been shown to fade by ≈ 1 mag since $z \approx 1$ (e.g., Lilly et al. 1995; Wolf et al. 2003; Faber et al. 2007), suggesting that there are fewer optically luminous late-type galaxies in the local universe than at $z = 1$.
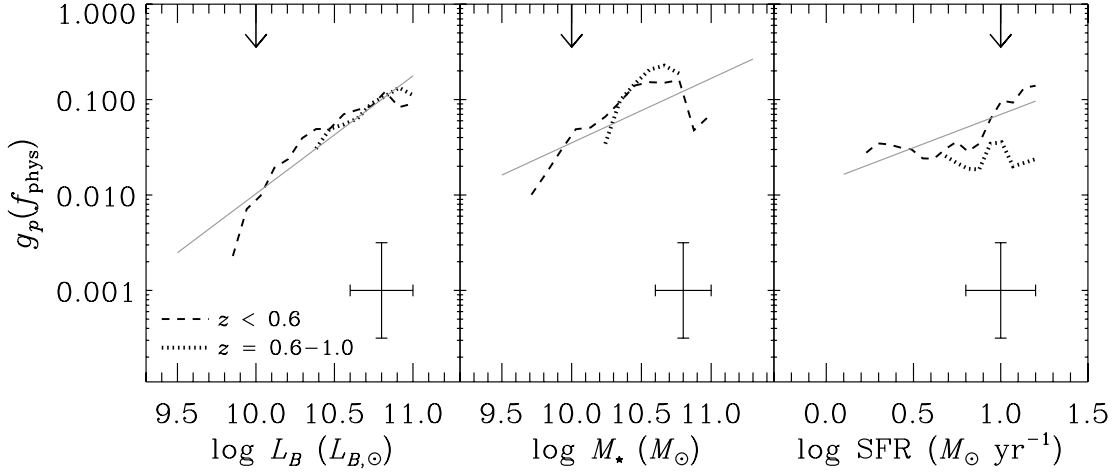
FIG. 14.—Cumulative AGN fraction $g_p(f_{phys})$ vs. L_B (left), $M_\star$ (middle), and SFR (right) for late-type galaxies with $L_{2-8\,keV} \gtrsim 10^{41.5}$ ergs s^{-1} at $z < 0.6$ (dashed curves) and $z = 0.6-1$ (dotted curves). In each plot, we have indicated the best-fit relation (solid line), which is calculated using all galaxies with $L_{2-8\,keV} \gtrsim 10^{41.5}$ ergs s^{-1} and $z < 0.6$. The downward-pointing arrows indicate which values of f_{phys} were chosen for computing g_0 in eq. (8). For reference, the bin sizes of f_{phys} used to compute each value of $g_p(f_{phys})$ and the typical errors of $g_p(f_{phys})$ have been indicated in the lower right-hand corner of each plot.

$L_{0.5-2\,keV}$(contam) of each stacked sample using the following summation:

$$L_{2-8\,keV}(\text{contam}) = \sum_i f_{U,i} \times L_{2-8\,keV,i}, \qquad (9)$$

where the summation is over all bins of $\Delta \log L_{2-8\,keV} = 0.5$ in the range $\log L_{2-8\,keV} = 39-45$. We converted each value of $L_{2-8\,keV}$(contam) to estimated values of $L_{0.5-8\,keV}$(contam) and $L_{0.5-2\,keV}$(contam) by assuming the contaminating AGN emission roughly follows an X-ray SED described by a power law. In order to constrain the average photon index of the power law, we stacked all X-ray–detected AGNs in our stacked samples with 0.5–8 keV luminosities below 10^{42} ergs s^{-1}. For these AGNs, we find a stacked effective photon index of $\Gamma_{eff} = 0.97 \pm 0.03$. If the intrinsic value of the photon index is $\Gamma = 2$, at the median redshift of our main sample ($z_{median} = 0.5$), $\Gamma_{eff} \approx 1$ corresponds to an intrinsic X-ray column density of $N_H \approx (1-2) \times 10^{22}$ cm^{-2}. If we assume $\Gamma_{eff} = 1$ describes well the effective SED of the X-ray–undetected AGNs in our stacked sample, we find that AGN contamination can account for $\approx 1\%-30\%$ (median of $\approx 5\%$) of the 0.5–8 keV emission from our stacked samples, suggesting that AGNs are not providing a significant contribution to our stacked results. We note that the X-ray SED used in this calculation has an important effect on the overall estimate of the AGN contamination. Since our estimates for contamination in the 0.5–8 keV and 0.5–2 keV bandpasses decrease as Γ_{eff} decreases, the amount of contamination in our samples may be underestimated if our choice of Γ_{eff} is too flat; however, we find that for conservative choices of Γ_{eff} (i.e., $\Gamma_{eff} \lesssim 2$) that are representative of even unobscured AGNs (for reference, see Fig. 5), the AGN contamination remains low ($\lesssim 40\%$) and has no material effect on our results.

It is also worth noting that if there exists a large population of intrinsically luminous yet heavily obscured AGNs in our high-redshift galaxy samples that are X-ray–undetected in the CDFs, then our conclusions above could be somewhat different. If such a population were present and had significant influence on our stacked results, then we would expect to find stacked X-ray spectra that were relatively flat ($\Gamma_{eff} \lesssim 1$); however, as discussed in § 5.1, we find that very few of our stacked samples could have such flat spectra in our stacked samples, suggesting that such a population, if present, does not have a strong effect on our results.

In Table 2 (cols. [25]–[27]), we have provided the estimated fractional AGN contribution to each stacked sample [i.e., $L_{E_1-E_2}$(contam)/$L_{E_1-E_2}$] for the FB, SB, and HB using the technique described above and an assumed $\Gamma_{eff} = 1$. We find that the estimated AGN contamination is most significant for galaxy samples with large values of L_B, $M_\star$, and SFR.

6. EXTENSION TO DISTANT LYMAN BREAK GALAXIES

As noted in § 1, the global star formation rate density has been observed to increase with redshift out to $z \sim 1-1.5$. Investigations of the most distant LBGs at $z \sim 2-7$ show that the star formation density peaks around $z \approx 1-3$ and gradually declines toward higher redshifts (e.g., Steidel et al. 1999; Giavalisco 2002; Giavalisco et al. 2004b; Bouwens et al. 2004, 2005; Dickinson et al. 2004). To investigate whether the mean X-ray activity from normal late-type galaxies follows a similar trend, we study the X-ray properties of a sample of $z = 3.01 \pm 0.24$ LBGs, which were identified as U-band "dropouts" through the GOODS project (see Lehmer et al. 2005a for details).

We filtered the GOODS $z \sim 3$ LBG sample (Lee et al. 2006) to include only LBGs that (1) were within the central $\approx 4.0'$ of the ≈ 2 Ms CDF-N and ≈ 1 Ms CDF-S, and (2) had rest-frame B-band luminosities that were similar to the most optically luminous $[L_B = (3-20) \times 10^{10}\,L_{B,\odot}]$ $z = 0-1.4$ late-type galaxies used in this study. B-band luminosities were calculated by applying k-corrections to the z_{850}-band flux (from GOODS), where k-corrections were derived using an SED appropriate for LBGs (see § 2.2 of Lehmer et al. 2005a for details). We found that 85 $z \sim 3$ LBGs from the Lehmer et al. (2005a) sample satisfied these two selection criteria.

We identified three X-ray–detected LBGs, which all had $L_{2-8\,keV} \gtrsim 10^{43}$ ergs s^{-1}. Due to their high X-ray luminosities, we classified these sources as obvious AGNs. After removing these three X-ray–detected AGNs from our $z \sim 3$ LBG sample, we performed X-ray stacking analyses as described in § 4.2. We found a significant (3.7 σ) detection in the 0.5–2 keV bandpass, which corresponds roughly to rest-frame 2–8 keV emission. Assuming an intrinsic power-law X-ray spectrum with a photon index of $\Gamma = 2$, we found a mean 0.5–8 keV luminosity of $L_X = (4.9 \pm 1.4) \times 10^{41}$ ergs s^{-1} for our $z \sim 3$ LBGs, a value that agrees well with previous studies (e.g., Lehmer et al. 2005a; Laird et al. 2006).
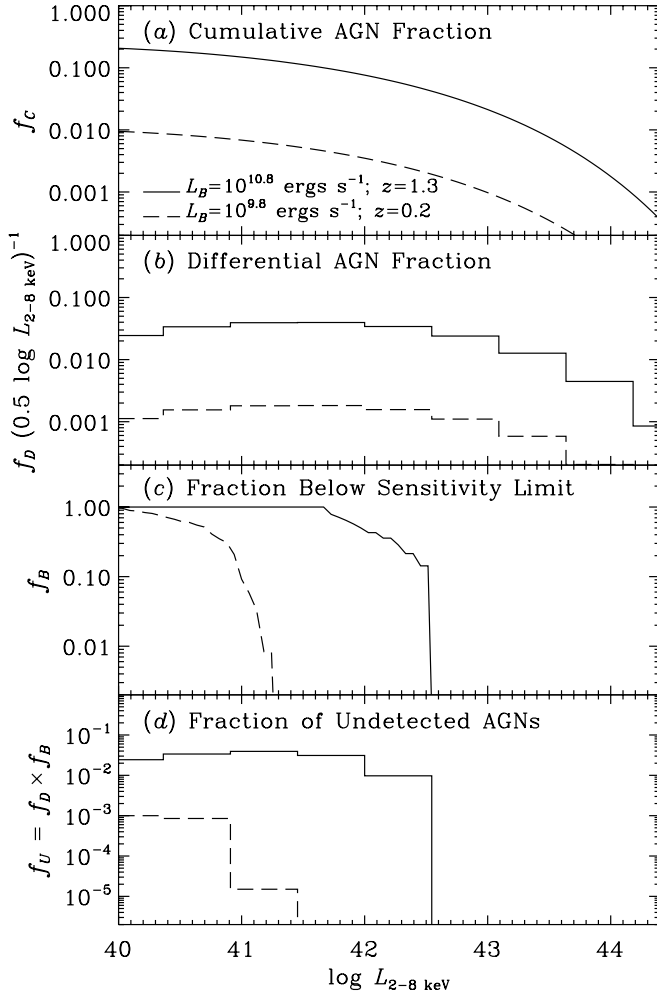
FIG. 15.—(a) Cumulative AGN fraction (i.e., the fraction of galaxies harboring an AGN with a 2–8 keV luminosity of $L_{2-8\,keV}$ or greater), f_C, vs. log $L_{2-8\,keV}$ for two of our stacked samples: $z \approx 0.2$ galaxies with $L_B = 10^{9.5}-10^{10}\,L_{B,\odot}$ (dashed curve) and $z \approx 1.3$ galaxies with $L_B = 10^{10.5}-10^{11.3}\,L_{B,\odot}$ (solid curve). Each curve was computed following eq. (8). (b) Differential AGN fractions (i.e., the fraction of galaxies harboring an AGN in discrete bins of width $\Delta \log L_{2-8\,keV} = 0.5$), f_D, vs. log $L_{2-8\,keV}$. (c) Fraction of late-type galaxies for which we could *not* have detected an AGN with a 2–8 keV luminosity of $L_{2-8\,keV}$, f_B, vs. log $L_{2-8\,keV}$. (d) Fraction of galaxies harboring AGNs in our optically luminous faded samples that would remain undetected due to sensitivity limitations, $f_U = f_D \times f_B$, vs. log $L_{2-8\,keV}$; these galaxies would not have been removed from our stacking analyses.

Since our LBGs reside in the high-redshift universe, AGN contamination is expected to have a more significant effect on these results than it did for our $z = 0-1.4$ late-type galaxies. The median X-ray luminosity detection limit is $\approx 8 \times 10^{41}$ ergs s^{-1} and $\approx 10^{43}$ ergs s^{-1} for the 0.5–2 keV and 2–8 keV bandpasses, respectively. To estimate the AGN contamination, we followed the approach outlined in § 5.2, which made use of the 2–8 keV luminosity dependent AGN fraction (f_C). In Figure 12 (*filled stars*), we show the X-ray luminosity dependent AGN fraction $g_{L,LBG}(L_{2-8\,keV})$ for $z \sim 3$ LBGs. We note that at $L_{2-8\,keV} \gtrsim 10^{43}$ ergs s^{-1}, the cumulative AGN fraction for $z \sim 3$ LBGs is a factor of $\approx 3-4$ times larger than that computed for our $z = 0-1$ late-type galaxy sample with similar optical luminosities. Using the functional form for f_C presented in equation (8), but with a $\approx 3-4$ times larger normalization factor for $z \sim 3$ LBGs [i.e., $g_{0,LBGs} \approx (3-4)g_0$], we find that AGN emission may plausibly account for $\approx 50\%-70\%$ of the stacked 0.5–2 keV counts.
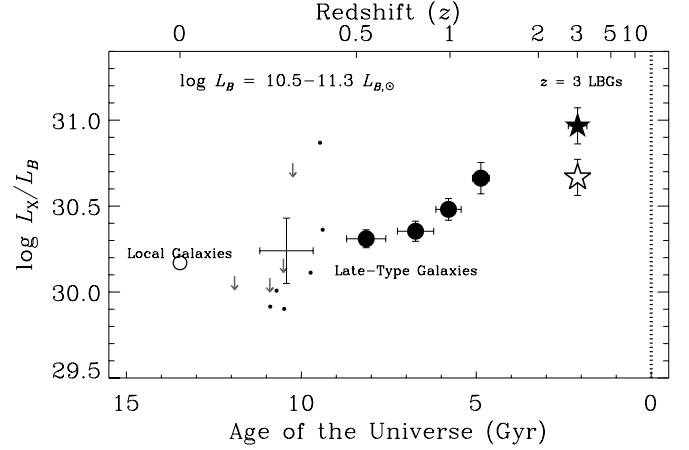

FIG. 16.—Logarithm of the X-ray–to–B band mean luminosity ratio log L_X/L_B vs. the age of the universe (for our adopted cosmology, the current age of the universe is 13.47 Gyr) for star-forming galaxies with $L_B = (3-20) \times 10^{10}\,L_{B,\odot}$. For reference, redshift has been plotted along the top axis. We have included mean values of L_X/L_B for the S01 local sample of late-type galaxies (*open circles*), our stacked samples at $z \approx 0.5-1.4$ (*large filled circles*), and $z \sim 3$ LBGs that were both uncorrected (*filled star*) and corrected (*open star*) for AGN contamination. At $z \approx 0.1-0.4$, we have plotted L_X/L_B for individual late-type galaxies from our main sample (*small filled circles and upper limits*); the mean values and errors for these galaxies, computed using ASURV, have been indicated.

In Figure 16, we show the X-ray–to–B-band mean luminosity ratio for $L_B = (3-20) \times 10^{10}\,L_{B,\odot}$ star-forming galaxies (i.e., late-type galaxies and LBGs) as a function of the age of the universe. Together, these data span $\approx 85\%$ of cosmic history (i.e., out to $z \sim 3$). As presented in § 5.1, L_X/L_B shows significant evolution over the redshift range $z = 0-1.4$, and after correcting for AGN contamination, we find that L_X/L_B is similar for $z \sim 3$ LBGs and $z = 1.4$ late-type galaxies. This result suggests that the non-AGN X-ray emission for the most luminous star-forming galaxies may flatten near $z \approx 1.4-3$, which has been predicted roughly from simulations of how the normal-galaxy X-ray emission is expected to respond due to global changes in the star formation rate density (e.g., Ghosh & White 2001).

To test whether the L_X-SFR correlation is similar for $z \sim 3$ LBGs as we found for late-type galaxies at $z = 0-1.4$, we approximated absorption-corrected SFRs for the $z \sim 3$ LBGs using UV-band emission. These SFRs were approximated following SFR $= 9.8 \times 10^{-11}\gamma L_{UV}$, where $\gamma \approx 6$ is the absorption-correction factor (see Giavalisco et al. 2004b). As described in § 3.3, we approximated the UV luminosity following $L_{UV} = 3.3\nu l_\nu(2800\,\text{Å})$; however, here $l_\nu(2800\,\text{Å})$ was derived using our adopted LBG SED. We find that the mean SFR for optically luminous $z \sim 3$ LBGs is $\approx 60\,M_\odot$ yr^{-1}. After correcting the mean stacked X-ray luminosity for AGN contamination, we find an X-ray–to–SFR ratio of log L_X/SFR $\approx 39.4-39.6$, which is suggestively lower than its value for $z = 0-1.4$ late-type galaxies (i.e., log L_X/SFR $= 39.87 \pm 0.04$). We note, however, that the estimation of the mean SFR for these galaxies is based solely on the 2800 Å emission and is therefore highly uncertain; further constraints on the mean infrared luminosity of these sources would help considerably. For reference, in Figure 11 we have plotted log SFR versus log L_X for the $z \sim 3$ LBGs both uncorrected (*filled star*) and corrected (*open star*) for AGN contamination.

It is interesting to note that the AGN-corrected LBG sample appears to have L_X and SFR values similar to those of local ULIRGs, which are relatively X-ray underluminous for their derived SFRs. PR07 suggest that galaxies with SFRs that begin

to exceed $\gtrsim 50$–$100\ M_\odot$ yr^{-1}, similar to the ULIRGs, may have X-ray properties that are completely dominated by HMXBs. In such systems, other X-ray–emitting populations that may normally be significant in more quiescent galaxies (e.g., LMXBs, hot gas, supernovae and their remnants, etc.) would collectively contribute only a negligible fraction of the total X-ray emission, thus causing the overall galaxies to appear X-ray underluminous compared with the L_X-SFR correlation. We note, however, that our results presented in § 5.1 suggest that HMXBs likely dominate the X-ray emission from galaxies with SFRs much lower than those of ULIRGs. Another possibility is that as the absorption within the most actively star-forming galaxies increases with SFR (see discussion in § 5.1), the X-ray emission from point-source populations may become significantly obscured. Deep X-ray observations of local LIRGs and ULIRGs with *Chandra* and *XMM-Newton* have found significant X-ray absorption in their point-source populations (see, e.g., Lira et al. 2002; Zezas et al. 2002, 2003), thus providing some support for this possibility. Future investigations into the nature of the X-ray populations of ULIRGs could help resolve this issue.

7. SUMMARY AND FUTURE WORK

We have investigated the X-ray emission from 2568 normal late-type galaxies over the redshift range $z = 0$–1.4 that lie within the Chandra Deep Fields (CDFs). Our late-type galaxy sample was constructed primarily using color-magnitude diagrams, which incorporated rest-frame $U - V$ color and absolute V-band magnitudes, to isolate blue late-type galaxies (see § 2 for details). In total, 225 ($\approx 9\%$) of our late-type galaxies were detected individually in the X-ray band. Based on X-ray and optical spectral properties, X-ray–to–optical flux ratios, the correlation between X-ray luminosity and star formation rate, and comparisons between infrared and radio properties, we infer that 121 ($\approx 53\%$) of the X-ray–detected late-type galaxies are dominated by AGN emission. The remaining 104 X-ray–detected galaxies had X-ray and multiwavelength properties consistent with those of normal late-type galaxies with X-ray emission dominated by X-ray binaries (HMXBs and LMXBs). To study the X-ray emission and evolution from large representative populations of late-type galaxies (i.e., including the X-ray–undetected sources), we utilized X-ray stacking analyses of galaxy populations with AGN candidates removed. We stacked normal-galaxy samples that were selected via their rest-frame B-band luminosity (L_B), stellar mass ($M_\star$), and star formation rate (SFR) in redshift bins (see § 5.1). Furthermore, we compared these results with those found for a sample of $z \sim 3$ LBGs from Lehmer et al. (2005a). In the points below, we summarize our key findings:

1. We obtained significant detections in the 0.5–2 keV and 0.5–8 keV bandpasses for all of our stacked samples. We estimated that LMXBs and low-level AGNs provide only low-level contributions to the stacked X-ray emission from our samples and that HMXBs constitute the dominant X-ray–emitting component. Therefore, for these galaxies the X-ray emission is tracing primarily star formation activity. Normal late-type galaxy samples selected via L_B and $M_\star$ show significant (at the >99.9% confidence level) evolution in their average X-ray properties from $z = 0$ to 1.4. For the most optically luminous ($L_B \approx 5 \times 10^{10}\ L_{B,\odot}$) and massive ($M_\star \approx 3 \times 10^{10}\ M_\odot$) late-type galaxies at $z = 1.4$, L_X/L_B and $L_X/M_\star$ are measured to be larger than their local values by factors of ≈ 2–4 and ≈ 7–13, respectively.

2. We find that late-type galaxies of lower stellar mass generally have larger X-ray–to–stellar mass mean ratios ($L_X/M_\star$) than their higher mass analogs. Over $z \approx 0.2$–1, galaxies with

$M_\star \approx 6 \times 10^9\ M_\odot$ are a factor of ≈ 2–3 times more X-ray luminous per unit stellar mass than galaxies with $M_\star \approx 3 \times 10^{10}\ M_\odot$.

3. We characterized the X-ray properties of 888 24 μm–detected late-type galaxies in our sample. The 24 μm data allowed us to select galaxy samples selected via their SFRs. For these samples, we found that the X-ray luminosity is well predicted by a constant L_X-to-SFR ratio, similar to the L_X-SFR correlation reported by previous authors (e.g., PR07). This implies that the L_X-SFR correlation holds out to at least $z = 0.5$, 1, and 1.4 for galaxies with SFR ≈ 2, 10, and 50 $M_\odot$ yr^{-1}, respectively, and supports the idea that the strong X-ray evolution observed for normal late-type galaxies selected via L_B and $M_\star$ is likely due to strong changes in SFR.

4. The X-ray properties of our most optically luminous [$L_B = (3$–$20) \times 10^{10}\ L_{B,\odot}$] late-type galaxies at $z = 1.4$ are comparable to those for $z \sim 3$ LBGs with similar optical luminosities, once X-ray–undetected AGN contamination in the LBG population has been accounted for. This suggests that there may plausibly be a flattening in the L_X/L_B-z relation for optically luminous star-forming galaxies between $z \sim 1.4$ and 3. We estimate a mean SFR of $\approx 60\ M_\odot$ yr^{-1} for these LBGs. We find that the observed mean X-ray luminosity is suggestively underluminous based on the L_X-SFR correlation prediction; this result is similar to that found for local ULIRGs with comparable SFRs.

The above results can be improved greatly through (1) the study of late-type galaxy populations in other existing multi-wavelength extragalactic survey fields that contain *Chandra* observations, (2) additional observations of the CDFs to even better sensitivity levels than are currently available, and (3) observations with future X-ray missions with imaging capabilities that are complementary to those of *Chandra*.

The areal footprint of the CDF regions used in this study totals ≈ 0.18 deg^2 (see § 2.1 for details), which severely limits the number of galaxies being studied at $z \lesssim 0.2$. The redshift range $z = 0$–0.2 spans ≈ 2.5 Gyr of cosmic look-back time, compared with the ≈ 6.6 Gyr over $z = 0.2$–1.4 that we are most effectively studying above. Several complementary deep and wide extragalactic *Chandra* survey fields that have recently been conducted or are in progress can improve the present situation. Three such ideal survey fields are the ≈ 200 ks All-wavelength Extended Groth Strip International Survey (AEGIS; e.g., Nandra et al. 2005; Davis et al. 2007), the ≈ 50 ks *Chandra* Cosmic Evolution Survey (C-COSMOS; PI: M. Elvis; see also Scoville et al. 2007),[21] and the ≈ 5 ks NOAO Deep Wide-Field Survey (NDWFS; e.g., Murray et al. 2005).

Our study shows that identifying and removing contaminating AGNs is a crucial ingredient to studying the stacked X-ray properties of normal-galaxy samples (see § 5.2). In order to avoid significant levels of AGN contamination in shallower wide-area *Chandra* surveys such as AEGIS, C-COSMOS, and NDWFS, X-ray studies of normal galaxy populations must be limited to lower redshift intervals. If we require a detection limit of $L_{0.5–2\,\mathrm{keV}} = 10^{41.5}$ ergs s^{-1} over regions of each survey where the *Chandra* sensitivity is optimal (i.e., $\lesssim 6.0'$ from the *Chandra* aim points), then we estimate that AEGIS, C-COSMOS, and NDWFS could effectively be used to study normal late-type

---

[21] We note that the C-COSMOS observing strategy has been designed to have several overlapping ≈ 50 ks ACIS-I exposures; in these regions, the total exposure will reach ≈ 200 ks due to the overlapping exposures. However, the analyses presented in this paper utilize only high-quality *Chandra* imaging at off-axis angles of $\lesssim 6.0'$ (see § 2.1 for additional justification), where there is very little overlap in the C-COSMOS *Chandra* pointings. We therefore do not consider the overlapping regions of the C-COSMOS exposures in this discussion. For additional information regarding C-COSMOS, see http://cfa-www.harvard.edu/hea/cos/C-COSMOS.html.

galaxy populations at redshifts less than ≈ 0.5, ≈ 0.25, and ≈ 0.1, respectively. When factoring in the areal coverage of these fields, we estimate that AEGIS and C-COSMOS will contain ≈ 250–350 late-type galaxies with $L_B \gtrsim 3 \times 10^9$ $L_{B,\odot}$ at $z = 0.1$–0.2 (i.e., a factor of ≈ 3 larger than the CDFs) and that AEGIS, C-COSMOS, and NDWFS taken together will have ≈ 100–250 similar galaxies at $z \lesssim 0.1$ (i.e., a factor of ≈ 22 times larger than the CDFs). Studying these galaxy populations would significantly improve constraints on the X-ray properties of $z \lesssim 0.2$ late-type galaxies.

Deeper *Chandra* observations of the CDFs would provide additional insight into the X-ray properties of the normal late-type galaxy populations presented in this study and enable us to extend our analyses to higher redshifts. Typical galaxies in our sample have mean X-ray luminosities of $L_X \approx 10^{39.5}$–10^{40} ergs s^{-1}. In the ≈ 2 Ms CDF-N, where our *Chandra* sensitivity is greatest, we expect that galaxies with $L_X \approx 10^{39.5}$ ergs s^{-1} should be detectable out to $z \approx 0.2$. Out of the 11 late-type galaxies with $L_B \gtrsim 10^9$ $L_{B,\odot}$ at $z \lesssim 0.2$, we find X-ray detections for 8 of them ($\approx 72\%$). Deeper *Chandra* observations over the CDFs will allow for the detection of such galaxies out to progressively higher redshifts. For *Chandra* exposures of ≈ 5 Ms and ≈ 10 Ms, a source with $L_X \approx 10^{39.5}$ ergs s^{-1} should be detectable out to $z \approx 0.3$ and $z \approx 0.4$, respectively. If we pessimistically assume an X-ray detection fraction of $\approx 70\%$, we estimate that ≈ 30 and ≈ 50 normal galaxies would be detected individually for each respective deep exposure. The individual detection of these galaxies would allow for improved constraints on both the X-ray luminosity functions of normal late-type galaxies at higher redshifts and the low-luminosity AGN contributions to our stacked signals. At higher redshifts, an ≈ 5 Ms and ≈ 10 Ms *Chandra* exposure would enable us to effectively perform studies of normal late-type galaxies, similar to those presented in this paper, out to $z \approx 2$ and $z \approx 2.5$, respectively. Such a data set would provide, for the first time, a reliable constraint on the X-ray emission from normal star-forming galaxies near the peak of the global star formation rate density at $z \approx 1.5$–3.

In addition to the improvement that additional *Chandra* observations could provide, future X-ray missions such as *XEUS* and *Generation-X*[22] should enable new scientific investigations of distant normal galaxies. *XEUS* will be able to place significant spectral constraints for sources with 0.5–2 keV fluxes down to $\approx 10^{-17}$ ergs cm^{-2} s^{-1}, a level fainter than many of the average fluxes derived from our samples. *Generation-X* is planned to provide imaging with $\approx 0.1''$ per resolution element and will easily probe to flux levels of $\approx 10^{-19}$ ergs cm^{-2} s^{-1} ($L_X \approx 5 \times 10^{38}$ ergs s^{-1} at $z = 1$). At these levels, the first detailed investigations of the evolution of the normal late-type galaxy X-ray luminosity function can be performed effectively out to $z \gtrsim 1$ without confusion problems due to the crowding of large numbers of sources. Furthermore, these observations will allow for new constraints to be placed on the X-ray populations of all normal galaxies in the observable universe that are offset by more than ≈ 0.8 kpc from their host-galaxy nuclei.

[22] For additional information regarding the future X-ray missions *XEUS* and *Generation-X*, see http://www.rssd.esa.int/XEUS/ and http://genx.cfa.harvard.edu, respectively.

REFERENCES

Afonso, J., Mobasher, B., Koekemoer, A., Norris, R. P., & Cram, L. 2006, AJ, 131, 1216
Alexander, D. M., Aussel, H., Bauer, F. E., Brandt, W. N., Hornschemeier, A. E., Vignali, C., Garmire, G. P., & Schneider, D. P. 2002, ApJ, 568, L85
Alexander, D. M., et al. 2003, AJ, 126, 539
Alonso-Herrero, A., et al. 2006, ApJ, 640, 167
Baldry, I. K., Glazebrook, K., Brinkmann, J., Ivezić, Ž., Lupton, R. H., Nichol, R. C., & Szalay, A. S. 2004, ApJ, 600, 681
Barger, A. J., Cowie, L. L., & Wang, W.-H. 2007, ApJ, 654, 764
Barger, A. J., et al. 2003, AJ, 126, 632
Bauer, F. E., Alexander, D. M., Brandt, W. N., Hornschemeier, A. E., Vignali, C., Garmire, G. P., & Schneider, D. P. 2002a, AJ, 124, 2351
Bauer, F. E., Alexander, D. M., Brandt, W. N., Schneider, D. P., Treister, E., Hornschemeier, A. E., & Garmire, G. P. 2004, AJ, 128, 2048
Bauer, F. E., Brandt, W. N., & Lehmer, B. 2003, AJ, 126, 2797
Bauer, F. E., et al. 2002b, AJ, 123, 1163
Bell, E. F. 2003, ApJ, 586, 794
Bell, E. F., & de Jong, R. S. 2001, ApJ, 550, 212
Bell, E. F., McIntosh, D. H., Katz, N., & Weinberg, M. D. 2003, ApJS, 149, 289
Bell, E. F., Zheng, X. Z., Papovich, C., Borch, A., Wolf, C., & Meisenheimer, K. 2007, ApJ, 663, 834
Bell, E. F., et al. 2004a, ApJ, 608, 752
———. 2004b, ApJ, 600, L11
———. 2005, ApJ, 625, 23
Blanton, M. R., et al. 2003, ApJ, 594, 186
Borch, A., et al. 2006, A&A, 453, 869
Bouwens, R. J., Illingworth, G. D., Thompson, R. I., & Franx, M. 2005, ApJ, 624, L5
Bouwens, R. J., et al. 2004, ApJ, 616, L79
Brand, K., et al. 2005, ApJ, 626, 723
Brandt, W. N., & Hasinger, G. 2005, ARA&A, 43, 827

Brandt, W. N., Hornschemeier, A. E., Schneider, D. P., Alexander, D. M., Bauer, F. E., Garmire, G. P., & Vignali, C. 2001, ApJ, 558, L5
Bundy, K., et al. 2006, ApJ, 651, 120
Caldwell, J. A. R., et al. 2005, ApJS, submitted (astro-ph/0510782)
Capak, P., et al. 2004, AJ, 127, 180
Church, M. J., & Bałucińska-Church, M. 2001, A&A, 369, 915
Cohen, J. G. 2003, ApJ, 598, 288
Colbert, E. J. M., Heckman, T. M., Ptak, A. F., Strickland, D. K., & Weaver, K. A. 2004, ApJ, 602, 231
Colbert, J. W., et al. 2006, ApJ, 648, 250
Cowie, L. L., Songaila, A., Hu, E. M., & Cohen, J. G. 1996, AJ, 112, 839
Daddi, E., et al. 2007a, ApJ, 670, 156
———. 2007b, ApJ, 670, 173
Dale, D. A., Helou, G., Contursi, A., Silbermann, N. A., & Kolhatkar, S. 2001, ApJ, 549, 215
Davis, M., et al. 2007, ApJ, 660, L1
de Vaucouleurs, G., de Vaucouleurs, A., Corwin, H. G., Buta, R. J., Paturel, G., & Fouque, P. 1991, Third Reference Catalog of Bright Galaxies (Berlin: Springer)
Dickinson, M., et al. 2004, ApJ, 600, L99
Doane, N. E., Sanders, W. T., Wilcots, E. M., & Juda, M. 2004, AJ, 128, 2712
Donley, J. L., Rieke, G. H., Pérez-González, P. G., Rigby, J. R., & Alonso-Herrero, A. 2007, ApJ, 660, 167
Fabbiano, G. 1989, ARA&A, 27, 87
———. 2006, ARA&A, 44, 323
Fabbiano, G., Kim, D.-W., & Trinchieri, G. 1992, ApJS, 80, 531
Fabbiano, G., & Shapley, A. 2002, ApJ, 565, 908
Faber, S. M., et al. 2007, ApJ, 665, 265
Fazio, G. G., et al. 2004, ApJS, 154, 10
Fioc, M., & Rocca-Volmerange, B. 1997, A&A, 326, 950
Freeman, P. E., Kashyap, V., Rosner, R., & Lamb, D. Q. 2002, ApJS, 138, 185
Gawiser, E., et al. 2006, ApJS, 162, 1

Georgakakis, A., Georgantopoulos, I., Stewart, G. C., Shanks, T., & Boyle, B. J. 2003, MNRAS, 344, 161

Georgakakis, A., Rowan-Robinson, M., Babbedge, T. S. R., & Georgantopoulos, I. 2007, MNRAS, 377, 203

Georgantopoulos, I., Georgakakis, A., & Koulouridis, E. 2005, MNRAS, 360, 782

Ghosh, P., & White, N. E. 2001, ApJ, 559, L97

Giacconi, R., et al. 2002, ApJS, 139, 369

Giavalisco, M. 2002, ARA&A, 40, 579

Giavalisco, M., et al. 2004a, ApJ, 600, L93

———. 2004b, ApJ, 600, L103

Gilfanov, M. 2004, MNRAS, 349, 146

Gilfanov, M., Grimm, H.-J., & Sunyaev, R. 2004a, Nucl. Phys. B Proc. Suppl., 132, 369

———. 2004b, MNRAS, 347, L57

Gilli, R., et al. 2003, ApJ, 592, 721

Gilmore, G., King, I., & van der Kruit, P. 1990, The Milky Way as a Galaxy (Sausalito: University Science Books)

Grazian, A., et al. 2006, A&A, 449, 951

Grimm, H.-J., Gilfanov, M., & Sunyaev, R. 2002, A&A, 391, 923

———. MNRAS, 339, 793

Hammer, F., Puech, M., Chemin, L., Flores, H., & Lehnert, M. D. 2007, ApJ, 662, 322

Häussler, B., et al. 2007, ApJS, 172, 615

Hogg, D. W., Baldry, I. K., Blanton, M. R., & Eisenstein, D. J. 2002a, preprint (astro-ph/0210394)

Hogg, D. W., et al. 2002b, AJ, 124, 646

———. 2004, ApJ, 601, L29

Hopkins, A. M. 2004, ApJ, 615, 209

Hornschemeier, A. E., et al. 2000, ApJ, 541, 49

———. 2002, ApJ, 568, 82 (H02)

———. 2003, AJ, 126, 575

Irwin, J. A., Athey, A. E., & Bregman, J. N. 2003, ApJ, 587, 356

Isobe, T., & Feigelson, E. 1990, BAAS, 22, 917

Jenkins, L. P., Roberts, T. P., Ward, M. J., & Zezas, A. 2005, MNRAS, 357, 109

Juneau, S., et al. 2005, ApJ, 619, L135

Kauffmann, G., et al. 2003a, MNRAS, 341, 54

———. 2003b, MNRAS, 346, 1055

Kennicutt, R. C., Jr. 1998, ARA&A, 36, 189

Kilgard, R. E., et al. 2005, ApJS, 159, 214

Kim, D.-W., et al. 2006, ApJ, 644, 829

Kroupa, P. 2001, MNRAS, 322, 231

Kroupa, P., Tout, C. A., & Gilmore, G. 1993, MNRAS, 262, 545

Labbé, I., et al. 2007, ApJ, 665, 944

Laird, E. S., Nandra, K., Adelberger, K. L., Steidel, C. C., & Reddy, N. A. 2005, MNRAS, 359, 47

Laird, E. S., Nandra, K., Hobbs, A., & Steidel, C. C. 2006, MNRAS, 373, 217

Lavalley, M., Isobe, T., & Feigelson, E. 1992, in ASP Conf. Ser. 25, Astronomical Data Analysis Software and Systems I, ed. D. M. Worrall, C. Biemesderfer, & J. Barnes (San Francisco: ASP), 245

Lee, K.-S., Giavalisco, M., Gnedin, O. Y., Somerville, R. S., Ferguson, H. C., Dickinson, M., & Ouchi, M. 2006, ApJ, 642, 63

Le Fèvre, O., et al. 2004, A&A, 428, 1043

Lehmer, B. D., et al. 2005a, AJ, 129, 1

———. 2005b, ApJS, 161, 21

———. 2006, AJ, 131, 2394

———. 2007, ApJ, 657, 681

Lilly, S. J., Le Fevre, O., Hammer, F., & Crampton, D. 1996, ApJ, 460, L1

Lilly, S. J., Tresse, L., Hammer, F., Crampton, D., & Le Fevre, O. 1995, ApJ, 455, 108

Lira, P., Ward, M. J., Zezas, A., & Murray, S. S. 2002, MNRAS, 333, 709

Liu, Q. Z., & Mirabel, I. F. 2005, A&A, 429, 1125

Liu, Q. Z., van Paradijs, J., & van den Heuvel, E. P. J. 2006, A&A, 455, 1165

Lockman, F. J. 2004, Soft X-Ray Emission from Clusters of Galaxies and Related Phenomena, ed. R. Lieu (Dordrecht: Kluwer), 111

Lonsdale, C. J., et al. 2003, PASP, 115, 897

Maccacaro, T., Gioia, I. M., Wolter, A., Zamorani, G., & Stocke, J. T. 1988, ApJ, 326, 680

Madau, P., Ferguson, H. C., Dickinson, M. E., Giavalisco, M., Steidel, C. C., & Fruchter, A. 1996, MNRAS, 283, 1388

McIntosh, D. H., et al. 2005, ApJ, 632, 191

McKee, C. F., & Williams, J. P. 1997, ApJ, 476, 144

Mignoli, M., et al. 2005, A&A, 437, 883

Mobasher, B., et al. 2004, ApJ, 600, L167

Moran, E. C., Filippenko, A. V., & Chornock, R. 2002, ApJ, 579, L71

Moy, E., Barmby, P., Rigopoulou, D., Huang, J.-S., Willner, S. P., & Fazio, G. G. 2003, A&A, 403, 493

Murray, S. S., et al. 2005, ApJS, 161, 1

Nandra, K., Mushotzky, R. F., Arnaud, K., Steidel, C. C., Adelberger, K. L., Gardner, J. P., Teplitz, H. I., & Windhorst, R. A. 2002, ApJ, 576, 625

Nandra, K., et al. 2005, MNRAS, 356, 568

———. 2007, ApJ, 660, L11

Noeske, K. G., et al. 2007a, ApJ, 660, L43

———. 2007b, ApJ, 660, L47

Norman, C., et al. 2004, ApJ, 607, 721

Olsen, L. F., et al. 2006, A&A, 456, 881

Papovich, C., & Bell, E. F. 2002, ApJ, 579, L1

Peng, C. Y., Ho, L. C., Impey, C. D., & Rix, H.-W. 2002, AJ, 124, 266

Pérez-González, P. G., et al. 2005, ApJ, 630, 82

Persic, M., & Rephaeli, Y. 2007, A&A, 463, 481 (PR07)

Persic, M., Rephaeli, Y., Braito, V., Cappi, M., Della Ceca, R., Franceschini, A., & Gruber, D. E. 2004, A&A, 419, 849

Peterson, K. C., Gallagher, S. C., Hornschemeier, A. E., Muno, M. P., & Bullard, E. C. 2006, AJ, 131, 133

Ptak, A., Griffiths, R., White, N., & Ghosh, P. 2001, ApJ, 559, L91

Ptak, A., Mobasher, B., Hornschemeier, A., Bauer, F., & Norman, C. 2007, ApJ, 667, 826

Ranalli, P., Comastri, A., & Setti, G. 2003, A&A, 399, 39

Ravikumar, C. D., et al. 2007, A&A, 465, 1099

Reddy, N. A., & Steidel, C. C. 2004, ApJ, 603, L13

Richards, E. A., Kellermann, K. I., Fomalont, E. B., Windhorst, R. A., & Partridge, R. B. 1998, AJ, 116, 1039

Rieke, G. H., et al. 2004, ApJS, 154, 25

Rix, H., et al. 2004, ApJS, 152, 163

Rosa-González, D., Burgarella, D., Nandra, K., Kunth, D., Terlevich, E., & Terlevich, R. 2007, MNRAS, 379, 357

Rovilos, E., Georgakakis, A., Georgantopoulos, I., Afonso, J., Koekemoer, A. M., Mobasher, B., & Goudis, C. 2007, A&A, 466, 119

Sanders, D. B., Mazzarella, J. M., Kim, D.-C., Surace, J. A., & Soifer, B. T. 2003, AJ, 126, 1607

Sasaki, M., Pietsch, W., & Haberl, F. 2003, A&A, 403, 901

Schiminovich, D., et al. 2005, ApJ, 619, L47

Schmitt, H. R., Calzetti, D., Armus, L., Giavalisco, M., Heckman, T. M., Kennicutt, R. C., Jr., Leitherer, C., & Meurer, G. R. 2006, ApJ, 643, 173

Scoville, N., et al. 2007, ApJS, 172, 1

Shapley, A., Fabbiano, G., & Eskridge, P. B. 2001, ApJS, 137, 139 (S01)

Shen, S., Mo, H. J., White, S. D. M., Blanton, M. R., Kauffmann, G., Voges, W., Brinkmann, J., & Csabai, I. 2003, MNRAS, 343, 978

Silverman, J. D., et al. 2008, ApJ, 675, 1025

Snellen, I. A. G., & Best, P. N. 2001, MNRAS, 328, 897

Soria, R., & Wu, K. 2003, A&A, 410, 53

Spergel, D. N., et al. 2003, ApJS, 148, 175

Stark, A. A., Gammie, C. F., Wilson, R. W., Bally, J., Linke, R. A., Heiles, C., & Hurwitz, M. 1992, ApJS, 79, 77

Steffen, A. T., Brandt, W. N., Alexander, D. M., Gallagher, S. C., & Lehmer, B. D. 2007, ApJ, 667, L25

Steidel, C. C., Adelberger, K. L., Giavalisco, M., Dickinson, M., & Pettini, M. 1999, ApJ, 519, 1

Strateva, I., et al. 2001, AJ, 122, 1861

Swartz, D. A., Ghosh, K. K., McCollough, M. L., Pannuti, T. G., Tennant, A. F., & Wu, K. 2003, ApJS, 144, 213

Szokoly, G. P., et al. 2004, ApJS, 155, 271

Tozzi, P., et al. 2006, A&A, 451, 457

Tzanavaris, P., & Georgantopoulos, I. 2008, A&A, in press (arXiv:0801.4381)

Tzanavaris, P., Georgantopoulos, I., & Georgakakis, A. 2006, A&A, 454, 447

Vanzella, E., et al. 2005, A&A, 434, 53

———. 2006, A&A, 454, 423

Wirth, G. D., et al. 2004, AJ, 127, 3121

Wolf, C., Meisenheimer, K., Rix, H.-W., Borch, A., Dye, S., & Kleinheinrich, M. 2003, A&A, 401, 73

Wolf, C., et al. 2004, A&A, 421, 913

Zezas, A., Fabbiano, G., Rots, A. H., & Murray, S. S. 2002, ApJS, 142, 239

Zezas, A., Ward, M. J., & Murray, S. S. 2003, ApJ, 594, L31

Zheng, X. Z., Bell, E. F., Papovich, C., Wolf, C., Meisenheimer, K., Rix, H.-W., Rieke, G. H., & Somerville, R. 2007, ApJ, 661, L41